J. Fluid Mech. (2019), *vol.* 862, *pp.* 696–731. © Cambridge University Press 2019
doi:10.1017/jfm.2018.940

The electrostatically forced Faraday instability: theory and experiments

Kevin Ward[1,2,†], **Satoshi Matsumoto**[3] **and Ranga Narayanan**[1,†]

[1]University of Florida, Department of Chemical Engineering, Gainesville, FL 32611, USA

[2]University of Lille, IEMN CNRS 8520, 59655, Lille, France

[3]Human Spaceflight Technology Directorate, Japan Aerospace Exploration Agency, Tsukuba, Ibaraki 305-8505, Japan

(Received 10 April 2018; revised 21 September 2018; accepted 20 November 2018; first published online 14 January 2019)

The onset of interfacial instability in two-fluid systems using a viscous, leaky dielectric model is studied. The instability arises as a result of resonance between the parametric frequency of an imposed electric field and the system's natural frequency. In addition to a rigorous model that uses Floquet instability analysis, where both viscous and charge effects are considered, this study also provides convincing validating experiments. In other results, it is shown that (a) the imposition of a periodic electrostatic potential acts to counter gravity and this countering effect becomes more effective if a DC voltage is also added, (b) a critical DC voltage exists at which the interface becomes unstable such that no parametric frequency is required to completely destabilize the interface and (c) the leaky dielectric model approaches a model for a perfect dielectric/perfect conductor pair as the conductivity ratio becomes large. It is also shown via experiments that parametric resonant instability using electrostatic forcing may be reliably used to estimate interfacial tension to sufficient accuracy.

Key words: Faraday waves, parametric instability, pattern formation

1. Introduction

The observation of patterns arising from resonance may be traced to Faraday (1831), who used a violin bow to excite the patterns via acoustic waves in sand and in fluid mixtures. These patterns typically appear subharmonic to the forcing frequency (Rayleigh 1883), and arise either in the form of standing waves or subcritical break-up of an interface (Douady 1990). Many resulting waveforms can be generated by controlling the system parameters, including triangular, hexagonal, square or striped structures (Müller 1993; Edwards & Fauve 1994; Kudrolli & Gollub 1996), or discretized competing waveforms (Ciliberto & Gollub 1985; Batson, Zoueshtiagh & Narayanan 2013*b*). As the instability itself arises from resonance, it can be excited by a variety of methods including mechanical forcing (Benjamin & Ursell 1954; Kumar & Tuckerman 1994), acoustic forcing (Boukra *et al.* 2009; Tsai & Tsai 2013;

† Email addresses for correspondence: klward3@ufl.edu, ranga@ufl.edu

https://doi.org/10.1017/jfm.2018.940 Published online by Cambridge University Press

Tsai *et al.* 2017) or even electrostatic forcing (Taylor & McEwan 1965; Briskman & Shaidurov 1968; Yih 1968).

The early theoretical work of Benjamin & Ursell (1954) demonstrated that a Mathieu equation would result when a two-fluid inviscid bilayer is subjected to mechanical oscillations. It was shown that the zones of stability alternate between subharmonic and harmonic responses. Early experiments, such as those by Abramson, Dodge & Kana (1965), Henderson & Miles (1990) and Tipton & Mullin (2004) utilized this model with relative success, by accounting for viscosity through the use of additional *ad hoc* damping terms. Troyon & Gruber (1971) theoretically investigated the stabilization of the Rayleigh–Taylor instability by imposing oscillatory forcing akin to that imposed for the Faraday instability using a viscous model, which supported previous work by Wolf (1970). Sterman-Cohen, Bestehorn & Oron (2017) previously conducted a similar analysis for vertically and horizontally oscillated Rayleigh–Taylor unstable thin films in the long-wave limit. Jacqmin & Duval (1988) further developed the viscous theoretical model for the mechanically forced Faraday instability by utilizing the Navier–Stokes equations in the absence of a mean gravitational acceleration. Kumar & Tuckerman (1994) developed a similar model which allowed for non-zero mean gravitational acceleration. This model was validated experimentally with great success by Bechhoefer *et al.* (1995) for the minimum thresholds in large geometries and by Batson *et al.* (2013*b*) for finite geometries allowing discretized modes through careful fluid selection and experimental procedures. Cerda & Tirapegui (1998) further explored the effects of viscosity on the mechanical system in order to delineate the mechanism for the production of standing waves in highly viscous systems.

Although research on the mechanically forced Faraday instability has been extensive, studies on promoting the instability through electrostatic forcing are less common. The first models for this method of forcing were produced by Taylor & McEwan (1965), Briskman & Shaidurov (1968) and Yih (1968). These models are the electrostatic analogues to the Benjamin & Ursell (1954) model for mechanically forced systems. Simplifying assumptions were made such as inviscid fluids and a perfect conductor–perfect dielectric pair, ultimately resulting, again, in a Mathieu equation. Bandopadhyay & Hardt (2017) recently extended these types of models to account for viscous effects. Early experiments were conducted by Devitt & Melcher (1965) utilizing high frequency fields to determine the stability thresholds between a dielectric fluid and air to great success. Iino, Suzuki & Ikushima (1985) and, more recently, Tsukahara, Tsuruta & Fujiwara (2013) intentionally excited Faraday waves using electrostatic oscillations in laterally constrained bilayer systems to correlate the observed resonant frequencies to the interfacial tension between the fluids. The aim of these works was not to predict or measure the stability threshold, but to experimentally determine resonant frequencies for a fixed forcing amplitude of the oscillatory voltage. Pontiga & Castellanos (1994) and Smorodin & Taraut (2010) have studied the effect of alternating electric fields on buoyancy convection problems. Khorshidi, Jalaal & Esmaeilzadeh (2011) have experimentally studied the use of constant electric fields to induce mixing between leaky dielectric fluids, and Ozen *et al.* (2006) have performed the linear stability analysis for a Poiseuille flow of two leaky dielectric fluids in the presence of a constant electric field.

The importance of charge accumulation on the interfaces between fluids is common to all of these research studies, and the accepted theoretical model for its description is the leaky dielectric model, initially given by Taylor (1966) and later presented by Melcher & Taylor (1969). This model is discussed extensively and applied to multiple

https://doi.org/10.1017/jfm.2018.940 Published online by Cambridge University Press

problems in the review article by Saville (1997). In short, the model is comprised of the typical equations of motion coupled with electromechanical stresses at the fluid interfaces resulting from an accumulation of charge, allowing for departure from the stresses that arrive in perfect conductor or perfect dielectric models. This model has been used extensively to investigate and explain various electrohydrodynamic phenomena (Pease & Russel 2002; Reddy & Esmaeeli 2009; Yang, Li & Xu 2017).

Most relevant to the current study is the work of Pease & Russel (2002) who conducted a linear stability analysis on a thin polymer film between two substrates with an air gap between the film and top substrate using the leaky dielectric model. The goal of the work was to delineate the mechanism for self-assembly patterns generated in lithography processes, where electrical fields arise naturally within the problem. Purposefully imposing a constant electric field can produce similar patterns, as shown, for example, by Dong, de Almeida & Tsouris (2001), Shankar & Sharma (2004), Craster & Matar (2005) and Tseluiko & Papageorgiou (2007). The effect of imposing an alternating electric field was examined by Roberts & Kumar (2009, 2010), who utilized the leaky dielectric model to investigate the additional control gained by employing AC fields over pillaring instabilities in thin polymer films by performing nonlinear simulations in the long-wave limit. These works effectively show that AC fields can be used to further tailor topographical expressions arising due to electrohydrodynamics for two and three-fluid films. The effect of viscoelasticity on this instability was later explored by Espin, Corbett & Kumar (2013) for both AC and DC fields. Gambhire & Thaokar (2010, 2012) also utilized linear stability analysis to study the effect of alternating electric fields on the system stability in leaky dielectric bilayers of infinite lateral and axial extent and also examine the role of conductivity on the resulting instabilities both theoretically and experimentally in the thin-film limit. These works disregard inertia in their analyses and Faraday resonance is not included in the physics. The stability of thin films in these studies relates to the effect of imposed electric fields, steady and periodic, on the Rayleigh–Taylor instability. The current work is focused on resonant instability and relaxes the thin-film assumptions so as to make it applicable to experiments of interest in this study.

Much as the work by Kumar & Tuckerman (1994) served to improve the Benjamin & Ursell (1954) model, this paper focuses on enhancing the Yih (1968) type models for electrostatically forced Faraday instability through the addition of viscosity and leaky dielectric properties for the fluids. The first aim of the current work is to introduce and explain a broad, rigorous model derived through linear stability analysis of the electrohydrodynamical equations for the prediction of purely electrostatically forced Faraday instability in two-fluid systems. The second aim is to provide experimental verification of this resonant instability. However, before introducing leaky dielectrics into the problem, we present a simpler derivation which is equivalent to an earlier model (Bandopadhyay & Hardt 2017) where the inviscid assumption alone is relaxed to highlight viscous effects. The derivation for the full model with the leaky dielectric and charge dynamics is then presented. This full model is complemented by experiments that were specifically designed to allow for the validation of the model. This study therefore represents the first attempt to have a realistic model on electrostatic resonant interfacial instability. It is also the first that provides clear experimental verification and validation of resonant forcing. An important outcome of the validating experiments is a novel way to measure the interfacial tension between fluids that may be subject to electrostatic forcing. One possible application of this new technique could be the measurement of interfacial tension between semiconductors and encapsulants, such as gallium arsenide and boron oxide.

https://doi.org/10.1017/jfm.2018.940 Published online by Cambridge University Press

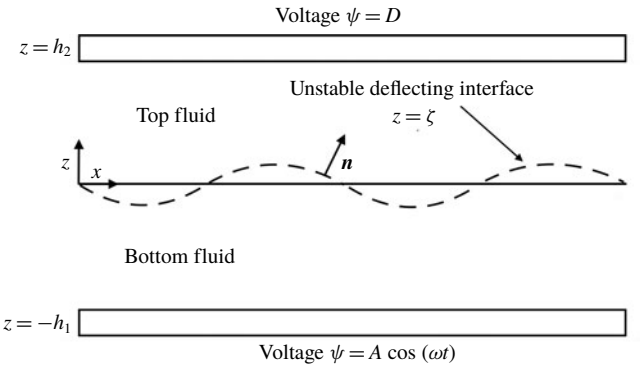


FIGURE 1. Schematic of two-fluid electrostatically oscillated system. The normal vector points into the upper fluid, and the interface is taken to be initially flat and located at $z = 0$. The voltage on the bottom electrode is oscillated with amplitude A and frequency ω, and the top electrode is held at a constant voltage D.

2. Theoretical models and calculations

Two sequential models are developed for the prediction of electrostatically forced Faraday instability thresholds. The first of these models is called the perfect conductor model, and is essentially an extension of the inviscid model derived by Yih (1968) (cf. appendix A for a re-derivation of the Yih model) to account for viscous effects. This model was also utilized in the recent work by Bandopadhyay & Hardt (2017), but is re-derived here in order to set the stage for the second more practically relevant model – one that includes charge dynamics at the interface and one that can be verified by experiments. The second model is called the leaky dielectric model and will be addressed in § 2.3. In the first model, the bottom fluid is taken to be a perfect conductor and the top fluid is taken to be a perfect dielectric. These assumptions greatly simplify the governing equations and allow for a simpler calculation due to the inherent decoupling of the perturbed voltage profiles with the perturbed hydrodynamic equations. We first present this simpler model to highlight the effect of viscosity on the instability thresholds. We then discuss the leaky dielectric model, in which both fluids are taken to be leaky dielectrics. The differences between the two models are described in the discussion of the second case.

2.1. *Perfect conductor model*

Two fluids of infinite lateral dimension are subject to an oscillatory voltage on electrodes located at the horizontal walls, located at $-h_1$ and h_2, as shown in figure 1. The upper wall is held at a constant voltage D and the lower wall at a voltage $A\cos(\omega t)$. The parameter D can take any value, including zero. Our view of the problem is this: D and ω are set while A is sequentially increased from zero until the fluid system enters a flow state, the base state being quiescent. The ultimate objective of the calculation is to plot the critical value of A versus ω for the onset of flow so as to make it relevant to experiments.

Taking the index 1 to be the bottom fluid and 2 to be the top fluid, we observe that the electrostatics in the top fluid in this model are governed by Laplace's equation for the voltage, given by

$$\nabla^2\psi_2 = 0, \tag{2.1}$$

https://doi.org/10.1017/jfm.2018.940 Published online by Cambridge University Press

and the bottom fluid is taken to have constant potential due to its infinite conductivity. The boundary conditions for ψ are taken as the two imposed voltages, *viz.*,

$$\psi_2 = D \tag{2.2}$$

and

$$\psi_2 = A\cos\omega t \tag{2.3}$$

at the top wall ($z = h_2$) and at the interface ($z = \zeta(x, t)$), respectively.

The hydrodynamic equations in both fluids are governed by the Navier–Stokes equations along with the continuity equation, given by

$$\rho_j\left(\frac{\partial \boldsymbol{V}_j}{\partial t} + \boldsymbol{V}_j \cdot \boldsymbol{\nabla}\boldsymbol{V}_j\right) = -\boldsymbol{\nabla}P_j + \mu_j\nabla^2\boldsymbol{V}_j - \rho_j g\boldsymbol{i}_z \tag{2.4}$$

and

$$\boldsymbol{\nabla}\cdot\boldsymbol{V}_j = 0, \tag{2.5}$$

where $\boldsymbol{V}$ is the fluid velocity, P is the pressure, μ is the viscosity, ρ is the density, g is gravitational acceleration and $j = 1, 2$ denotes the bottom and top fluid, respectively. The hydrodynamic description is completed by no-slip and no-penetration boundary conditions on the upper and lower walls and the following interface conditions (at $z = \zeta(x, t)$):

$$[[\boldsymbol{V}_j \cdot \boldsymbol{n}]] = 0, \tag{2.6}$$

$$[[\boldsymbol{V}_j \cdot \boldsymbol{t}]] = 0, \tag{2.7}$$

$$[[\boldsymbol{n}\cdot\boldsymbol{T}\cdot\boldsymbol{n}]] = \gamma 2H, \tag{2.8}$$

$$[[\boldsymbol{n}\cdot\boldsymbol{T}\cdot\boldsymbol{t}]] = 0, \tag{2.9}$$

along with the evolution equation for the interfacial deflection,

$$[[\rho_j(\boldsymbol{V}_j - \boldsymbol{U})\cdot\boldsymbol{n}]] = 0, \tag{2.10}$$

where $\boldsymbol{n}$ is the unit normal vector pointing into the light fluid, $\boldsymbol{t}$ is the unit tangent vector, $2H$ is twice the mean surface curvature, $\boldsymbol{U}\cdot\boldsymbol{n}$ is the interfacial speed and the double brackets $[[\phi_j]]$ represents $\phi_2 - \phi_1$.

The stress tensor $\boldsymbol{T}$ which appears in (2.8) and (2.9) is decomposed into two parts, a Maxwell stress and the hydrodynamic stress, *viz.*,

$$\boldsymbol{T} = \boldsymbol{T}^{Maxwell} + \boldsymbol{T}^{Hydrodynamic}, \tag{2.11}$$

where $\boldsymbol{T}^{Hydrodynamic}$ takes its usual form and $\boldsymbol{T}^{Maxwell}$ takes the form

$$\boldsymbol{T}^{Maxwell} = \epsilon\epsilon_0\boldsymbol{E}\boldsymbol{E} - \tfrac{1}{2}\epsilon\epsilon_0\boldsymbol{E}\cdot\boldsymbol{E}\boldsymbol{I}, \tag{2.12}$$

where $\boldsymbol{E} = -\boldsymbol{\nabla}\psi$ is the electric field, ϵ is the relative permittivity of the fluid, ϵ_0 is the permittivity of free space and $\boldsymbol{I}$ is the identity tensor. Due to the simplification of the electrical properties, the normal components of the Maxwell stress can be written as

$$[[\boldsymbol{T}^{Maxwell}\cdot\boldsymbol{n}]]\cdot\boldsymbol{n} = \tfrac{1}{2}[\epsilon_2\epsilon_0(-\boldsymbol{\nabla}\psi_2\cdot\boldsymbol{n})^2 - \epsilon_2\epsilon_0(-\boldsymbol{\nabla}\psi_2\cdot\boldsymbol{t}_1)^2 - \epsilon_2\epsilon_0(-\boldsymbol{\nabla}\psi_2\cdot\boldsymbol{t}_2)^2], \tag{2.13}$$

https://doi.org/10.1017/jfm.2018.940 Published online by Cambridge University Press

where $\boldsymbol{t}_1$ and $\boldsymbol{t}_2$ are unit tangent vectors. Within the perfect conductor model, there are no tangential component contributions to the Maxwell stress tensor. Thus, the velocity profiles can be solved in terms of the interface deflection, ζ, relying on the normal stress balance, i.e. (2.8), to close the problem. This approach closely follows that of the mechanically forced problem (Kumar & Tuckerman 1994), and the full derivation for the velocity profiles is given in appendix B.

In order to determine the stability conditions, we linearize the dependent variables about a stationary, non-deflecting interface as

$$\left.\begin{array}{c} \psi_2 = \psi_2^0 + \psi_2', \\ \zeta = \zeta', \\ \boldsymbol{V} = \boldsymbol{V}', \\ P = P^0 + P', \end{array}\right\} \tag{2.14}$$

where the superscript '0' represents the base state and the superscript '′' represents the perturbed state. Inserting (2.14) into the nonlinear equations, yields (at zeroth order)

$$\psi_2^0 = \frac{(D - A\cos\omega t)z}{h_2} + A\cos\omega t \tag{2.15}$$

and

$$\frac{\mathrm{d}P_j^0}{\mathrm{d}z} = -\rho_j g, \tag{2.16}$$

which shows that the base state potential varies linearly through the top fluid while the base state pressure gradient is balanced by gravity.

Next, we collect the terms of order '′' and separate variables using the traditional Floquet expansion:

$$\phi'(x, z, t) = \mathrm{e}^{\mathrm{i}kx}\ \tilde{\phi}(z, t) = \mathrm{e}^{\mathrm{i}kx} \sum_{n=-\infty}^{\infty} \mathrm{e}^{(\sigma+\mathrm{i}(\alpha+n\omega))t}\hat{\phi}_n(z), \tag{2.17}$$

where ϕ' is each of the perturbed dependent variables, σ is the growth rate, k is the wavenumber and α can take the value of zero or $\omega/2$ to allow for both harmonic and subharmonic responses. We then map the dependent variables at the interface back to $z = 0$ (Johns & Narayanan 2002) to obtain the perturbed electrostatic domain equation and the accompanying boundary conditions:

$$\left(\frac{\partial^2}{\partial z^2} - k^2\right)\tilde{\psi}_2 = 0, \tag{2.18}$$

$$\tilde{\psi}_2|_{z=h_2} = 0, \tag{2.19}$$

$$\left(\tilde{\psi}_2 + \tilde{\zeta}\frac{\partial \psi_2^0}{\partial z}\right)\bigg|_{z=0} = 0. \tag{2.20}$$

Inserting the base state voltage contributions from (2.15), expanding fully with (2.17) and solving for the perturbed voltage profile, we get (dropping hats)

$$\psi_{n2} = \frac{D\zeta_n - \dfrac{A}{2}(\zeta_{n-1} + \zeta_{n+1})}{h_2}(\sinh kz \coth kh_2 - \cosh kz), \tag{2.21}$$

https://doi.org/10.1017/jfm.2018.940 Published online by Cambridge University Press

which is equivalent to the Yih (1968) result even in the presence of viscosity due to the absence of viscosity within the electrostatic equations and the fact that the coupling between the electrostatic and hydrodynamic equations is only a one-way coupling when utilizing the perfect conductor model assumptions. Upon determination of the velocity profiles as shown in appendix B, the normal stress balance becomes

$$\left[\left[\rho_j(\sigma+\mathrm{i}(\alpha+n\omega)+3\mu_j k^2)\frac{\mathrm{d}W_{nj}}{\mathrm{d}z}-\mu_j\frac{\mathrm{d}^3W_{nj}}{\mathrm{d}z^3}\right]\right]+((\rho_2-\rho_1)g-\gamma k^2)k^2\zeta_n=-k^2\tau^{Maxwell}, \tag{2.22}$$

where W_{nj} is the vertical velocity component of the jth fluid, and subscript n is the index from (2.17). The variable, $\tau^{Maxwell}$, is defined by first taking the perturbation of (2.13) at first order, yielding the contribution of the Maxwell stress to the right-hand side of the normal stress balance, *viz.*,

$$([[\boldsymbol{T}^{Maxwell}\cdot\boldsymbol{n}]]\cdot\boldsymbol{n})'=\frac{\mathrm{d}\psi_2'}{\mathrm{d}z}\frac{\partial\psi_2^0}{\partial z}=\eta(D^2-2DA\cos\omega t+A^2\cos^2\omega t)\zeta', \tag{2.23}$$

where $\eta=(k\epsilon_2\epsilon_0\coth kh_2/h_2^2)$. Expanding with (2.17), applying the double angle formula, and dropping hats yields

$$\tau^{Maxwell}=\eta\left(D^2\zeta_n-DA(\zeta_{n-1}+\zeta_{n+1})+\frac{A^2}{4}(\zeta_{n-2}+2\zeta_n+\zeta_{n+2})\right). \tag{2.24}$$

Substitution into (2.22) and rearranging yields the final normal stress balance:

$$\begin{aligned}\left[\left[\rho_j(\sigma+\mathrm{i}(\alpha+n\omega)+3\mu_j k^2)\frac{\mathrm{d}W_{nj}}{\mathrm{d}z}-\mu_j\frac{\mathrm{d}^3W_{nj}}{\mathrm{d}z^3}\right]\right]+((\rho_2-\rho_1)g+\eta D^2-\gamma k^2)k^2\zeta_n\\ =Ak^2\eta D(\zeta_{n-1}+\zeta_{n+1})-A^2\frac{k^2\eta}{4}(\zeta_{n-2}+2\zeta_n+\zeta_{n+2}).\end{aligned} \tag{2.25}$$

This expression is similar to that obtained for the mechanically forced Faraday instability (Kumar & Tuckerman 1994), with additional constant voltage terms and a modified time dependent forcing, here with both harmonic and twice harmonic components, arising from $\cos^2(\omega t)$. To consider neutral stability, we set σ to zero and then cast (2.25) as a polynomial eigenvalue problem with the form

$$B_n\zeta_n=CA\zeta_n+EA^2\zeta_n, \tag{2.26}$$

where B_n is a coefficient of the A independent terms and where C and E are the coefficients of A and A^2 terms, respectively. It is first important to note that within (2.26) we seek the critical values of A, i.e. the amplitude of the imposed oscillatory voltage. It is also important to note that both C and E are purely real. The reality conditions inherent to (2.17) are the same as those found in mechanical Faraday instability calculations for the ζ_{-1} terms, i.e. $\zeta_{-1}=\bar{\zeta}_1$ for $\alpha=0$ and $\zeta_{-1}=\bar{\zeta}_0$ for $\alpha=(\omega/2)$ along with the conditions for the ζ_{-2} terms $\zeta_{-2}=\bar{\zeta}_2$ for $\alpha=0$ and $\zeta_{-2}=\bar{\zeta}_1$ for $\alpha=(\omega/2)$. Here, the overbar indicates complex conjugates. To enforce the reality conditions, equation (2.26) can be separated into its real and complex parts, producing the final matrix equation governing the system stability:

$$\bar{\boldsymbol{B}}\bar{\zeta}=A\bar{\boldsymbol{C}}\bar{\zeta}+A^2\bar{\boldsymbol{E}}\bar{\zeta}, \tag{2.27}$$

where the matrices $\bar{\boldsymbol{B}}$, $\bar{\boldsymbol{C}}$ and $\bar{\boldsymbol{E}}$ are shown in appendix C.

https://doi.org/10.1017/jfm.2018.940 Published online by Cambridge University Press

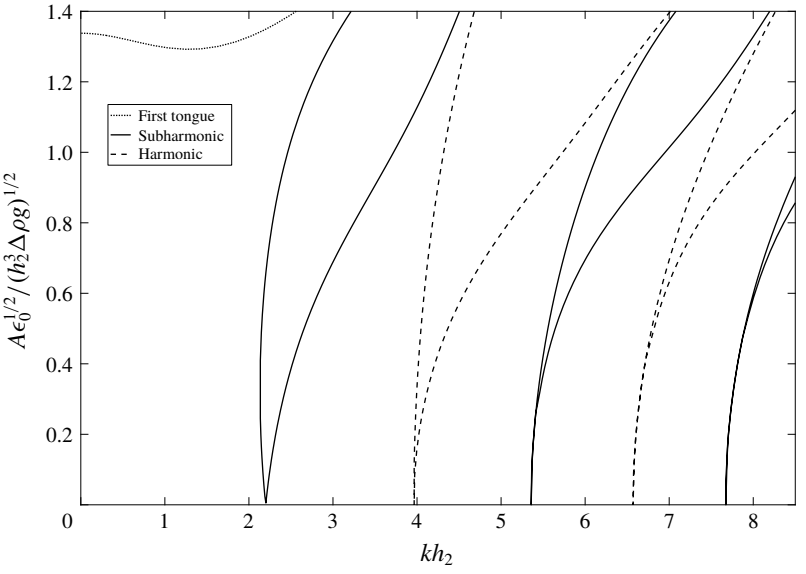


FIGURE 2. Scaled amplitude versus wavenumber for $D = 5000$ V calculated from the inviscid perfect conductor model. Alternating subharmonic and harmonic tongues are obtained when $D \neq 0$. Fluid parameters are $\rho_1 = 1000$ kg m^{-3}, $\rho_2 = 1.225$ kg m^{-3}, $h_1 = h_2 = 6$ mm, $\epsilon_2 = 1.00059$, $\gamma = 0.07275$ kg s^{-2} and $\omega = 25$ Hz.

For the current study, the index n was typically truncated at a value of 12. Including higher n values within the calculation added computational time and did not significantly alter the results. This polynomial eigenvalue problem is then solved using the 'polyeig' command within Matlab®, where the lowest, positive eigenvalue calculated is the critical amplitude, A, for the input frequency, ω, wavenumber, k and α value of either $\alpha = 0$ or $\alpha = (\omega/2)$. Such a calculation yields the lowest of the critical amplitudes, A, the corresponding wavenumber, k, and the harmonic nature of the response.

2.2. *Calculations for the perfect conductor model*

The inviscid electrostatically forced Faraday instability produces a Mathieu equation as shown by Yih (1968) and re-derived for the reader's convenience in appendix A. Figure 2 shows the results from the eigenvalue problem arising from the Mathieu equation cast into the familiar A versus k form for comparison to the upcoming viscous results. The figures are given in scaled form, where the voltage scale arises from (2.25) and the wavenumber is scaled by the height of the insulating fluid. The calculations are performed assuming the properties of water and air. Alternating subharmonic and harmonic tongues similar to those seen in mechanically forced Faraday instability problems (Benjamin & Ursell 1954) are found for $D \neq 0$, and the minimum threshold amplitude of each tongue is zero at the resonance points.

The addition of viscosity into the problem also results in alternating subharmonic and harmonic tongues when $D \neq 0$. Predictably, the minimum threshold of each tongue is finite, and increases with increasing wavenumber due to increased viscous damping from the choppier modes. In the case of $D = 0$, for both viscous and inviscid fluids only harmonic tongues can be obtained. This is due to the fact that the voltage

https://doi.org/10.1017/jfm.2018.940 Published online by Cambridge University Press

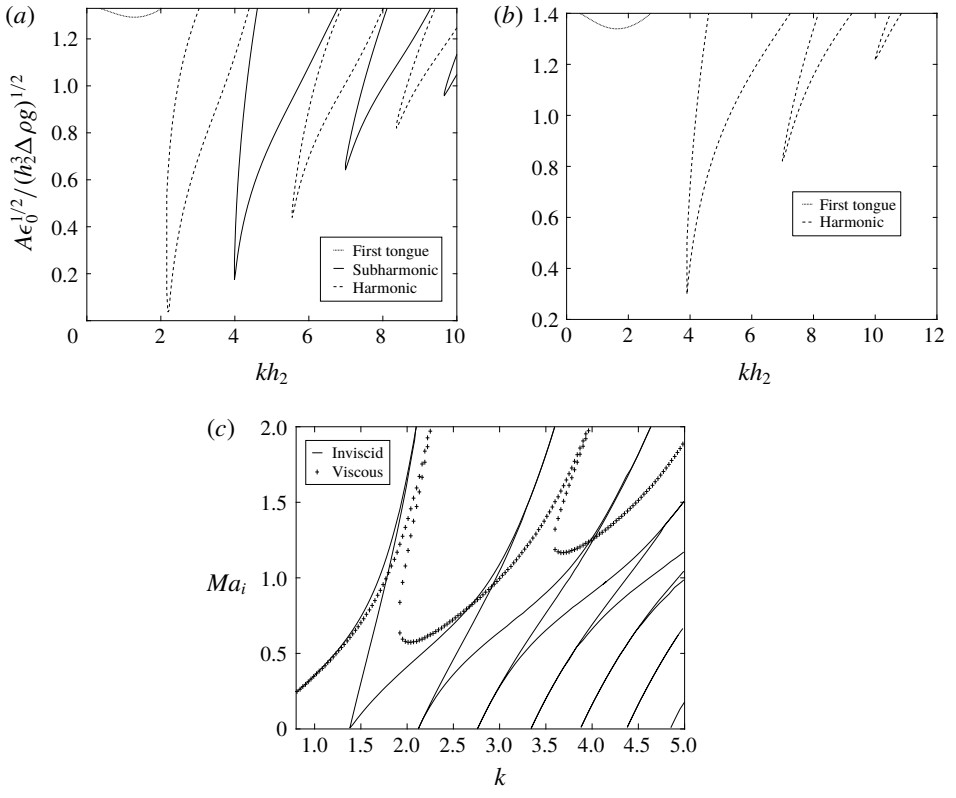


FIGURE 3. Scaled A versus k for both (a) $D = 5000$ V and (b) $D = 0$. Fluid parameters are $\mu_1 = 0.001$ kg ms^{-1}, $\mu_2 = 1.983 \times 10^{-5}$ kg ms^{-1} and other parameters equivalent to those in figure 2. Alternating subharmonic and harmonic tongues are seen when $D \neq 0$, while only harmonic tongues are observable when $D = 0$. (c) Reproduction of figure 3(a) of Bandopadhyay & Hardt (2017). The current model is able to recover the previously reported results in addition to the first tongue, not reported earlier. Fluid parameters and Ma_i are those given and defined by Bandopadhyay & Hardt (2017).

enters into the normal stress balance only as a squared term, i.e. $\cos^2(\omega t)$. When $D = 0$ is imposed, the $\cos(\omega t)$ terms vanish from (2.23), leaving only $\cos^2(\omega t)$ terms coming from the electrostatic forcing. The squared nature of these terms gives rise to a periodic forcing that is twice harmonic with the imposed frequency. In this case, the lowest possible response frequency is half of this forcing, therefore harmonic with the imposed frequency. However if $D \neq 0$ is set, the forcing consists of $\cos(\omega t)$ and $\cos^2(\omega t)$ terms. This allows the response to contain a subharmonic component as well as a harmonic component. Figure 3(a,b) shows the stability tongues for both cases, i.e. $D \neq 0$ and $D = 0$, now for the case of viscous fluids. In addition, figure 3(c) shows that the model is able to recover the Bandopadhyay & Hardt (2017) results in both the inviscid and viscous cases after rescaling.

Another peculiar characteristic of the electrostatic forcing comes in the form of an additional tongue, labelled in figure 3 as 'first tongue', which does not behave in the same manner as the others. This tongue is harmonic in nature, and specifically arises from the non-periodic stress terms that can be seen in (2.27). This tongue is not reported by Bandopadhyay & Hardt (2017), though this region may prove to be

https://doi.org/10.1017/jfm.2018.940 Published online by Cambridge University Press

important in certain circumstances where low wavenumbers can be accessed. These terms have two origins: one from the constant voltage on the top plate (D) and one from the non-periodic term generated through the use of the double angle formula. In the absence of periodic forcing, i.e. when $\omega = 0$, the 'first tongue' is in fact the only stability tongue, and is generated as a balance between the constant voltage stress term and $(\rho_2 - \rho_1)g - \gamma k^2$. This balance is given by

$$(\rho_2 - \rho_1)g - \gamma k^2 = -D^2\eta \tag{2.28}$$

for the perfect conductor model, where the value of D that satisfies this equation for a given k value is the critical value of D which is found on the first tongue. Equation (2.28) can be seen from the equation for the natural frequency in the Yih model (see appendix A) when the natural frequency is set equal to zero and is understandably independent of viscosity. The balance is similar in nature, albeit more complicated, for the leaky dielectric case. This tongue depicts the point where the time-independent components of the electrostatic stresses just commence to overwhelm the stabilizing effect of gravity and interfacial tension, allowing for destabilization of the interface.

The tongue still appears even in the absence of a constant voltage on the top plate when imposing a periodic forcing. The balance that leads to the critical amplitude, however, is not given by merely adding the term generated from the double angle formula to (2.28), as

$$(\rho_2 - \rho_1)g - \gamma k^2 = -D^2\eta - \frac{A^2\eta}{2}. \tag{2.29}$$

Instead, the physics arising from the oscillatory forcing alters the tongue's behaviour, such that it asymptotes with the first subharmonic tongue solution with increasing wavenumber. The eigenvalues of the tongue do correspond to those given by solving (2.29) for low wavenumbers, with the wavenumber range in which the two results correspond expanding with increasing frequency. This compares favourably with the accepted thought that applying a high frequency voltage oscillation produces almost identical behaviour to imposing a constant voltage drop. Since this tongue is always present, an inherent feature of the problem is a threshold amplitude below the first Faraday tongue for low wavenumbers. Contrast this to the mechanical Faraday problem (Kumar & Tuckerman 1994), where at very low wavenumbers the critical amplitude becomes extremely high. In the case of electrostatic forcing, at very low wavenumbers the critical amplitude is bounded by the first tongue.

Since the effects of the constant voltage offset and the constant terms arising from the periodic forcing are additive, it is easily seen that A_*, defined as the critical amplitude for the first tongue, decreases with increasing D. Figure 4 shows this effect for multiple values of D. The tongue will continue to shift to lower critical amplitudes until $(\rho_2 - \rho_1)g - \gamma k^2 + D^2\eta = 0$. For the fluid parameters tested (see figure captions), this phenomenon first occurs at $D = 14.47826$ kV. At this point, the system is unstable to one wavelength with any finite amplitude of oscillation. However, shorter wavelengths are able to be stabilized due to the hidden k inside the η parameter (see (2.23)).

Figure 5 shows the effect of changing D on the instability thresholds. It can clearly be seen that for subharmonic tongues, an increase in D causes the tongues to shift to higher wavenumber and lower critical amplitude. We also observe a narrowing of the

https://doi.org/10.1017/jfm.2018.940 Published online by Cambridge University Press

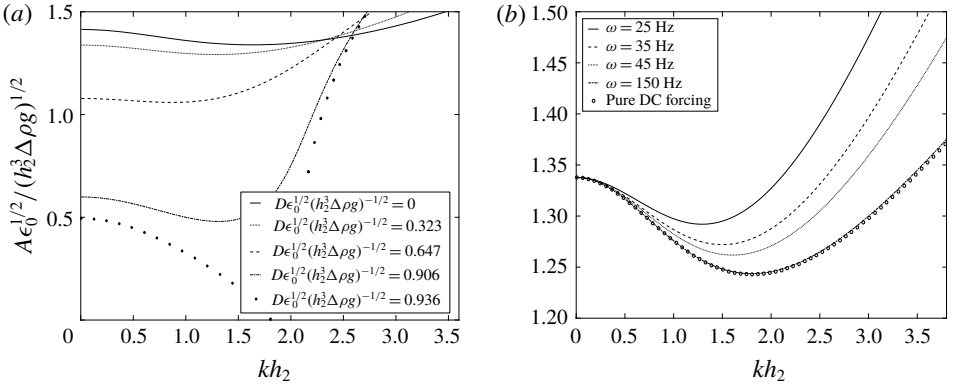


FIGURE 4. (*a*) Effect of D on the first harmonic tongue. The tongue shifts down in critical amplitude with increasing D, and first reaches a critical amplitude of 0 for $D \approx 14.48$ kV at $k = 301$ m^{-1} for the fluid parameters given in figure 3(*a*,*b*). (*b*) Effect of frequency on the first harmonic tongue. As frequency increases, the tongue approaches the pure DC electrostatic Rayleigh–Taylor instability solution. D is held at 5 kV for all tested frequencies.

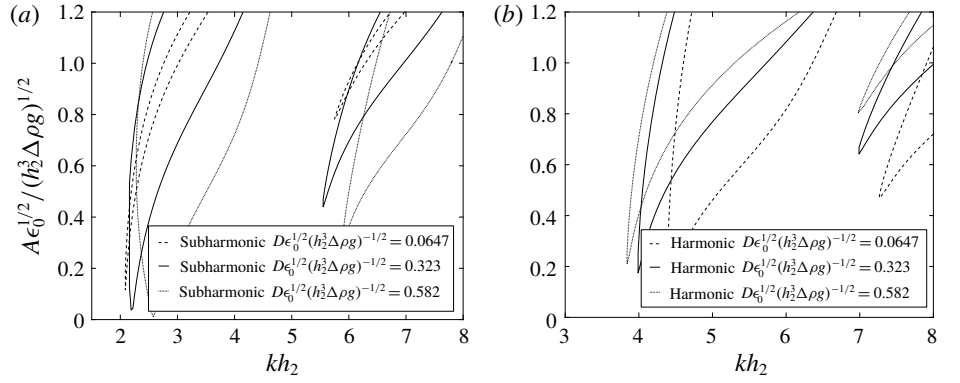


FIGURE 5. Effect of varying D on stability thresholds for both subharmonic (*a*) and harmonic (*b*) responses. Fluid properties are the same as those shown in figure 3(*a*). Increasing D has the general effect of widening the instability tongues and causing a shift to higher wavenumber and lower threshold amplitude. The first harmonic tongues discussed previously are omitted for clarity.

tongues with decreasing wavenumber. This trend continues as D decreases, eventually leading to extremely high threshold amplitudes as D approaches zero. Harmonic tongues also shift to higher wavenumber and lower critical amplitude with increasing D. However, this effect is much less pronounced than the subharmonic tongues. In addition, narrowing of the harmonic tongues occur to a much lesser extent with decreasing D. The increased effect of D on the subharmonic stability tongues again lends itself to the fact that subharmonic tongues are only achievable with finite D values, while harmonic tongues are achievable with $D = 0$.

https://doi.org/10.1017/jfm.2018.940 Published online by Cambridge University Press

2.3. *Leaky dielectric model*

The leaky dielectric model (LD) is also analysed through linear stability with the hydrodynamics aspect again following closely to the Kumar & Tuckerman (1994) model, modified by terms arising from the Maxwell stress (Saville 1997). This model is adapted by simultaneously solving the electrostatic equations to determine the Maxwell stress contributions, which are more complicated than those obtained in the perfect conductor model. Since the assumptions on the fluid electrical properties are relaxed, we can no longer decouple the perturbed voltage profiles with the perturbed hydrodynamic equations. Again, figure 1 shows the problem schematic, which is considered as a horizontally infinite two-fluid system.

Both fluids are now taken to be viscous, leaky dielectrics with no charged species present inside the fluid bodies, with both fluids exhibiting isotropic dielectric constants. Since the body force terms arising from the Maxwell stress are absent, the hydrodynamics in both fluids are again governed by the Navier–Stokes equations coupled with the continuity equation, given by (2.4)–(2.10), where the electrostatic forcing again enters into the problem only through the stress tensor at the interface (see (2.11)). In the LD model, the normal component of the Maxwell stress is given by

$$[[\boldsymbol{T}^{Maxwell}\cdot\boldsymbol{n}]]\cdot\boldsymbol{n}=\tfrac{1}{2}[[\epsilon_j\epsilon_0(-\nabla\psi_j\cdot\boldsymbol{n})^2-\epsilon_j\epsilon_0(-\nabla\psi_j\cdot\boldsymbol{t}_1)^2-\epsilon_j\epsilon_0(-\nabla\psi_j\cdot\boldsymbol{t}_2)^2]] \quad (2.30)$$

and the leaky dielectric nature of the fluids now also allows tangential components of the Maxwell stress, *viz.*,

$$[[\boldsymbol{T}^{Maxwell}\cdot\boldsymbol{n}]]\cdot\boldsymbol{t}=-q\nabla\psi\cdot\boldsymbol{t}, \quad (2.31)$$

where q is the interfacial charge density.

The electrostatics in both fluids are now governed by Laplace's equation:

$$\nabla^2\psi_j=0 \quad (2.32)$$

with the boundary conditions

$$\psi_2=D \quad (2.33)$$

and

$$\psi_1=A\cos\omega t \quad (2.34)$$

at the top ($z=h_2$) and bottom ($z=-h_1$) walls, respectively. The interfacial conditions are given by

$$\psi_2=\psi_1 \quad (2.35)$$

and

$$q(x,y,t)=[[-\epsilon_j\epsilon_0\nabla\psi_j]]\cdot\boldsymbol{n} \quad (2.36)$$

and the problem specification is completed by the interfacial charge equation

$$\frac{\partial q}{\partial t}=q\boldsymbol{n}\cdot(\boldsymbol{n}\cdot\nabla)\boldsymbol{V}+q(\boldsymbol{U}\cdot\boldsymbol{n})2H-V_x\cdot\frac{\partial q}{\partial x}+[[\sigma_j\nabla\psi_j\cdot\boldsymbol{n}]] \quad \text{at } z=\zeta(x,t), \quad (2.37)$$

where V_x is the x-component of the velocity and σ_j is the electrical conductivity of fluid j.

https://doi.org/10.1017/jfm.2018.940 Published online by Cambridge University Press

The dependent variables are once again linearized about a quiescent, non-deflecting interface in the same manner as previously shown. Upon collection of the base state terms, the electrostatics domain equations become

$$\frac{\partial^2 \psi_j^0}{\partial z^2} = 0. \tag{2.38}$$

The base state boundary conditions are given by

$$\left.\begin{aligned} \psi_2^0 &= D \quad \text{at } z = h_2, \\ \psi_1^0 &= A\cos\omega t \quad \text{at } z = -h_1, \\ \psi_2^0 &= \psi_1^0 \quad \text{at } z = 0, \\ q^0 &= \left[\left[-\epsilon_0\epsilon_j \frac{\partial \psi_j}{\partial z}\right]\right] \quad \text{at } z = 0, \end{aligned}\right\} \tag{2.39}$$

and the base state charge evolution equation is

$$\frac{\partial q^0}{\partial t} = \left[\left[\sigma_j \frac{\partial \psi_j^0}{\partial z}\right]\right] \tag{2.40}$$

since the base state is quiescent. The base state is solved by first obtaining the voltage profiles in terms of q for both fluids, resulting in

$$\left.\begin{aligned} \psi_1^0 &= \frac{h_2(q^0 z + q^0 h_1 + \epsilon_0\epsilon_1 A\cos\omega t) + \epsilon_0\epsilon_2((D - A\cos\omega t)z + Dh_1)}{\epsilon_0(h_2\epsilon_1 + h_1\epsilon_2)}, \\ \psi_2^0 &= \frac{h_1(-q^0 z + q^0 h_2 + D\epsilon_0\epsilon_2) + \epsilon_0\epsilon_1(h_2 A\cos\omega t + z(D - A\cos\omega t))}{\epsilon_0(h_2\epsilon_1 + h_1\epsilon_2)}. \end{aligned}\right\} \tag{2.41}$$

We then assume that the base state charge density takes the form

$$q^0 = \hat{q} + \tilde{\bar{q}} e^{i\omega t} + \bar{q} e^{-i\omega t} \tag{2.42}$$

due to the periodic nature of the voltage profiles. Upon substitution of (2.41) and (2.42) into (2.40), evaluation of the derivatives, and combining like terms, the expression for q^0 is obtained by

$$\left.\begin{aligned} \hat{q} &= \frac{-D\epsilon_0(\epsilon_2\sigma_1 - \epsilon_1\sigma_2)}{h_2\sigma_1 + h_1\sigma_2} = F_1, \\ \tilde{\bar{q}} &= \frac{iA\epsilon_0(\epsilon_2\sigma_1 - \epsilon_1\sigma_2)}{2(h_2(\omega\epsilon_0\epsilon_1 + i\sigma_1) + h_1(\omega\epsilon_0\epsilon_2 + i\sigma_2))} = A\ F_2 \end{aligned}\right\} \tag{2.43}$$

and

$$\bar{q} = \frac{-iA\epsilon_0(\epsilon_2\sigma_1 - \epsilon_1\sigma_2)}{2(h_2(\omega\epsilon_0\epsilon_1 - i\sigma_1) + h_1(\omega\epsilon_0\epsilon_2 - i\sigma_2))} = A\ \bar{F}_2, \tag{2.44}$$

where F_1 and F_2 are constants only dependent on input parameters. It is easily seen that q^0 and therefore ψ_1^0 and ψ_2^0 are independent of x and vary periodically with the imposed forcing. It should be noted here that in the limit of $\sigma_1 \to \infty$, the base state voltage profiles approach those observed using the perfect conductor model.

https://doi.org/10.1017/jfm.2018.940 Published online by Cambridge University Press

The base state electrostatics are now completely known and thus the next step is to collect terms of order ‘′’, using (2.17) to obtain the perturbed domain equation

$$\left(\frac{\partial^2}{\partial z^2} - k^2\right)\tilde{\psi}_j = 0 \tag{2.45}$$

and its corresponding boundary conditions

$$\left.\begin{aligned} \tilde{\psi}_1 &= 0 \quad \text{at } z = -h_1, \\ \tilde{\psi}_2 &= 0 \quad \text{at } z = h_2, \\ \tilde{\psi}_1 + \tilde{\zeta}\frac{\partial \psi_1^0}{\partial z} &= \tilde{\psi}_2 + \tilde{\zeta}\frac{\partial \psi_2^0}{\partial z} \quad \text{at } z = 0 \end{aligned}\right\} \tag{2.46}$$

and

$$\tilde{q} = \left[\left[-\epsilon_0\epsilon_j\frac{\partial \tilde{\psi}_j}{\partial z}\right]\right] \quad \text{at } z = 0 \tag{2.47}$$

along with the perturbed interfacial charge equation

$$\frac{\partial \tilde{q}}{\partial t} = q^0\frac{\partial \tilde{W}_1}{\partial z} + \left[\left[\sigma_j\frac{\partial \tilde{\psi}_j}{\partial z}\right]\right], \tag{2.48}$$

where W is the z-component of the perturbed velocity.

The perturbed hydrodynamic equations follow the equations given in appendix B with changes only occurring in the tangential and normal components of the stress balance. The perturbed tangential stress balance becomes

$$\mu_2\left(\frac{\partial^2}{\partial z^2} + k^2\right)\tilde{W}_2 - \mu_1\left(\frac{\partial^2}{\partial z^2} + k^2\right)\tilde{W}_1 = q^0k^2\left(\tilde{\psi}_1 + \tilde{\zeta}\frac{\partial \psi_1^0}{\partial z}\right) \tag{2.49}$$

and the perturbed normal stress balance becomes

$$\begin{aligned} &\left[\left[\rho_j\left(\frac{\partial}{\partial t} + 3\mu_j k^2\right)\frac{\mathrm{d}\tilde{W}_j}{\mathrm{d}z} - \mu_j\frac{\partial^3 \tilde{W}_j}{\mathrm{d}z^3}\right]\right] + ((\rho_2 - \rho_1)g - \gamma k^2)k^2\tilde{\zeta} \\ &\quad = -k^2\epsilon_0\left(\epsilon_2\left(\frac{\partial \tilde{\psi}_2}{\mathrm{d}z}\frac{\partial \psi_2^0}{\partial z}\right) - \epsilon_1\left(\frac{\partial \tilde{\psi}_1}{\partial z}\frac{\partial \psi_1^0}{\partial z}\right)\right). \end{aligned} \tag{2.50}$$

The perturbed velocity and voltage profiles must be solved simultaneously due to their coupling, and thus the remainder of the derivation is performed symbolically. Equation (2.48) is used to eliminate $\tilde{q}$ from the perturbed voltage boundary conditions, and the resultant set of boundary condition equations for both voltage and velocity are fully expanded using (2.17) and solved symbolically and computationally using Mathematica®. The analysis follows identically to that given in § 2.1. Once obtained, the profiles are substituted into (2.50), combining terms with common orders of A. This results in two distinct cases: for $D = 0$,

$$\begin{aligned} U_1\zeta_n \;=\; &A^2(Y_2\zeta_n + Y_3\zeta_{n-2} + Y_4\zeta_{n+2}) + A^4(Y_5\zeta_n + Y_6\zeta_{n-2} + Y_7\zeta_{n+2} + Y_8\zeta_{n-4} + Y_9\zeta_{n+4}) \\ &+ A^6(Y_{10}\zeta_n + Y_{11}\zeta_{n-2} + Y_{12}\zeta_{n+2} + Y_{13}\zeta_{n-4} + Y_{14}\zeta_{n+4} + Y_{15}\zeta_{n-6} + Y_{16}\zeta_{n+6}), \end{aligned} \tag{2.51}$$

https://doi.org/10.1017/jfm.2018.940 Published online by Cambridge University Press

and for $D \neq 0$,

$$\begin{aligned} Y_1\zeta_n \;=\; & A(Z_2\zeta_{n-1} + Z_3\zeta_{n+1}) + A^2(Z_4\zeta_n + Z_5\zeta_{n-2} + Z_6\zeta_{n+2}) \\ & + A^3(Z_7\zeta_{n-1} + Z_8\zeta_{n+1} + Z_9\zeta_{n-3} + Z_{10}\zeta_{n+3}) \\ & + A^4(Z_{11}\zeta_n + Z_{12}\zeta_{n-2} + Z_{13}\zeta_{n+2} + Z_{14}\zeta_{n-4} + Z_{15}\zeta_{n+4}) \\ & + A^5(Z_{16}\zeta_{n-1} + Z_{17}\zeta_{n+1} + Z_{18}\zeta_{n-3} + Z_{19}\zeta_{n+3} + Z_{20}\zeta_{n-5} + Z_{21}\zeta_{n+5}) \\ & + A^6(Z_{22}\zeta_n + Z_{23}\zeta_{n-2} + Z_{24}\zeta_{n+2} + Z_{25}\zeta_{n-4} + Z_{26}\zeta_{n+4} + Z_{27}\zeta_{n-6} + Z_{28}\zeta_{n+6}) \end{aligned} \tag{2.52}$$

due to changes in terms found in the final stress balance with non-zero D. In these equations, single letters with subscript numbers represent constants dependent on the input parameters and n. These cases must be separately treated in order to build the final matrix equations in a similar manner to (2.27). Once these matrices are built, the final polynomial eigenvalue problem is solved by exporting the matrices to Matlab®, and again utilizing the 'polyeig' command, resulting in multiple eigenvalues. Observe that in the leaky dielectric model, the maximum degree of the polynomial eigenvalue problem is six, in contrast to the perfect conductor model where the maximum degree is two. The lowest positive, real eigenvalue is taken to be the critical amplitude which governs the system stability for the input k, ω, α and fluid parameters.

2.4. *Calculations for the leaky dielectric model*

Effect of conductivities, permittivities and a comparison with the perfect conductor model

Utilizing a leaky dielectric model introduces multiple new parameters that can influence the system stability. We start our analysis by examining the effect of conductivity. For the purposes of the current work, σ_2 was set to a fixed value of 3×10^{-15} S m^{-1} and σ_1 was adjusted over a wide range. The first important result is the saturation of the base state charge density upon reaching a high value of σ_1. Figure 6 shows the value of the real part of $\tilde{\tilde{q}}$ from (2.40) as a function of σ_1. For low values of σ_1, we observe an exponential dependence of $\tilde{\tilde{q}}$ on σ_1. However, this trend vanishes upon reaching values of $\sigma_1 \geqslant 10^{-8}$, where a saturation of $\tilde{\tilde{q}}$ is observed beyond which increasing conductivity no longer strongly influences $\tilde{\tilde{q}}$.

The term $\tilde{\tilde{q}}$ also exhibits a saturation in situations where $\sigma_1 < \sigma_2$. In fact, at the exact point of equality, shown by the dashed line in figure 6, the value of $\tilde{\tilde{q}}$ asymptotes and reverses sign. This is indicative that the sign of the base state charge is dependent on the initial orientation of the fluids with respect to their electrical conductivities. If the value of σ_2 were subsequently raised after lowering σ_1 to 3×10^{-15}, the base state charge would saturate with high σ_2 to the same value as shown for high σ_1 but with opposing sign, though this only occurs precisely when the permittivities of both fluids are equal.

It should be noted here that $\hat{q}$ exhibits similar behaviour, but saturates at a much lower σ_1 than $\tilde{\tilde{q}}$. Here, the base state values of $\tilde{\tilde{q}}$ and $\hat{q}$ upon saturation can be accurately predicted by setting (2.15) and the ψ_2 portion of (2.41) equal to each other and solving for q_0. This results in

$$q_0 = -\left(D - \frac{A}{2}(\mathrm{e}^{\mathrm{i}\omega t} + \mathrm{e}^{-\mathrm{i}\omega t})\right)\frac{\epsilon_0\epsilon_2}{h_2} \tag{2.53}$$

https://doi.org/10.1017/jfm.2018.940 Published online by Cambridge University Press

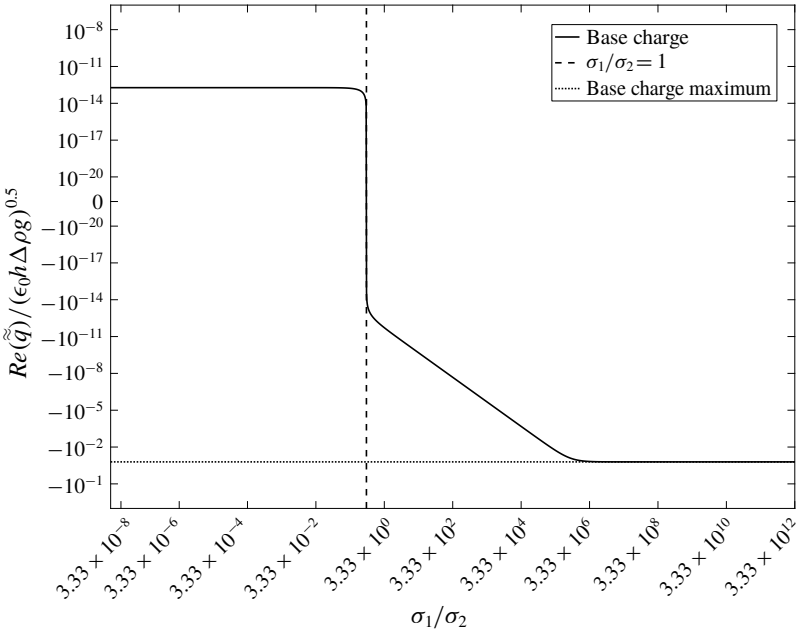


FIGURE 6. Effect of σ_1 on q_0. An exponential dependence is observed for low values of σ_1, but upon reaching $\sigma_1 = 10^{-8}$, q_0 saturates and is no longer strongly affected by increasing σ_1. Fluid parameters are the same as shown previously, assuming $\sigma_2 = 3 \times 10^{-15}$ S m^{-1} and $\epsilon_1 = \epsilon_2 = 1.00059$. $A = D = 5$ kV and $\omega = 25$ Hz.

which implies

$$\left.\begin{aligned} \hat{q} &= -\frac{D\epsilon_0\epsilon_2}{h_2}, \\ \tilde{\tilde{q}} &= \frac{A\epsilon_0\epsilon_2}{2h_2}, \end{aligned}\right\} \tag{2.54}$$

which is shown by the dotted line in figure 6. Once $\tilde{\tilde{q}}$ and $\hat{q}$ saturate, it is seen that the base state voltage profiles in both fluids yield the same results as the perfect conductor model. However, at $\sigma_1 < 10^{-8}$, a departure between the voltage profiles is observed. The implications of this phenomenon are shown in figure 7 for z values in the centre of each layer and at the interface.

Thus, we can conclude that the maximum value of the base state charge density and also the maximum amplitude of the base state voltage drop across the fluids are given by those values which satisfy the perfect conductor model. It can also be shown that decreasing the conductivity of the bottom fluid much lower than that of the top fluid causes the same phenomena to occur, assuming that the perfect conductor model is re-derived with the conducting fluid on top. This behaviour is indicative that the leaky dielectric model will give similar results to the perfect conductor model, provided the conductivity of the bottom fluid is very high. This should come as no surprise, as this stipulation is the very assumption that leads to the simplifications made in the perfect conductor model case.

Another behaviour, shown in figure 7(*d*), is that the voltage profiles saturate to lower values very quickly with decreasing σ_1 if the permittivity ratio, i.e. ϵ_1/ϵ_2 is high. The

https://doi.org/10.1017/jfm.2018.940 Published online by Cambridge University Press

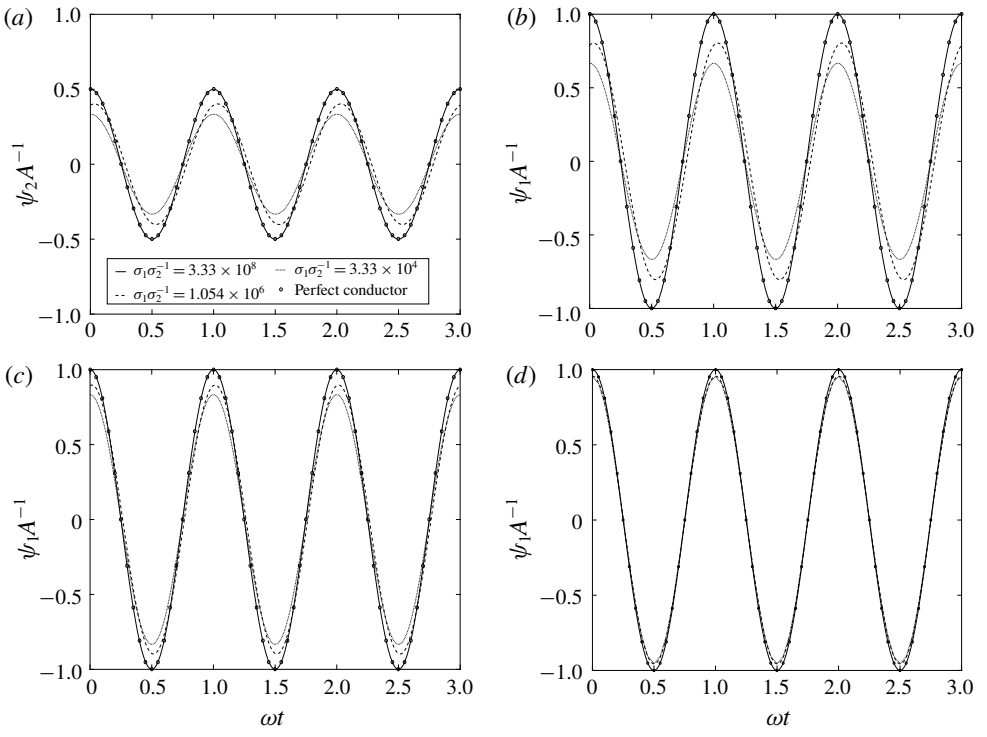


FIGURE 7. Effect of σ_1 on the base state voltage profiles in the centre of the top fluid (a), at the interface (b) and in the centre of the bottom fluid (c). It is clearly seen that as σ_1 increases, the voltage profiles approach those of the perfect conductor model. Fluid properties and ω are equivalent to those in figure 6 and $D = 0$. (d) The same properties as (c), with the exception that $\epsilon_1 = 10$. The base state voltage profiles saturate much more quickly with decreasing σ_1 if $\epsilon_1 \gg \epsilon_2$.

behaviour is similar within the top fluid and at the interface and thus the results are omitted for brevity. This results in an insensitivity to conductivity of the base state voltage profiles, and ultimately the system stability. The saturation values are given by those which are derived for the perfect dielectric model, obtained by setting q to zero in (2.36) and omitting (2.37).

Using the base state and corresponding perturbed state profiles, we now generate A versus k curves for the leaky dielectric model for comparison to those produced by the perfect conductor model. For high σ_1, as predicted, the leaky dielectric model yields results very similar to those seen in figure 3. However, upon lowering σ_1, we find a quick departure from the perfect conductor model. Figure 8(a) shows the effect of conductivity on the system stability, along with the corresponding perfect conductor model results for comparison.

Departure from the perfect conductor model

The departure in the Faraday tongues from the perfect conductor model arises quickly with decreasing conductivity of the bottom fluid. Typically, the stability tongues shift upward and to slightly lower wavenumber while maintaining their shapes. This behaviour is caused as the lower conductivity requires a higher imposed

https://doi.org/10.1017/jfm.2018.940 Published online by Cambridge University Press

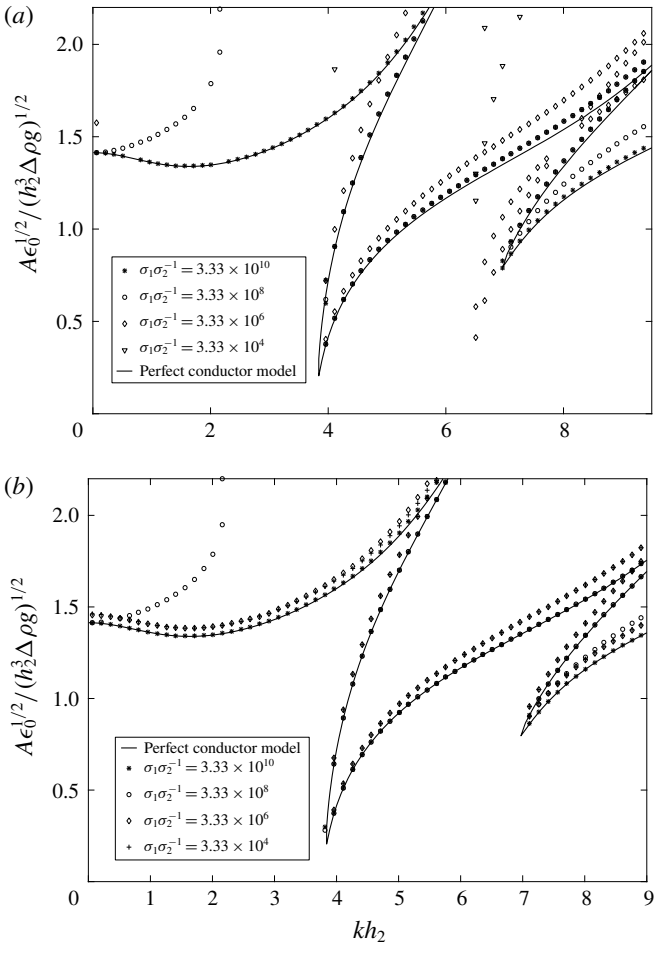


FIGURE 8. Stability thresholds for the leaky dielectric model assuming various conductivities for the bottom fluid. It is seen that a high conductivity will yield similar results to the perfect conductor model, but lowering the conductivity quickly causes a departure from this ideality. $\omega = 25$ Hz and the fluid properties are the same as those given in figure 3(*b*), along with $\sigma_2 = 3 \times 10^{-15}$ S m^{-1} and (*a*) $\epsilon_1 = 2$ or (*b*) $\epsilon_1 = 50$.

amplitude to generate the same interfacial stress due to voltage drops across the bulk. The exception to the rule can be seen in the case of $\sigma_1 = 10^{-8}$ S m^{-1}, where the second harmonic tongue decreases in threshold amplitude from the more conductive cases. This behaviour is presumably caused by the complex interaction between conductivity and permittivity, where terms multiplying higher orders of A, not seen in the perfect conductor model, begin to grow (see (2.26) and (2.51)). Thus, slight destabilization can be observed by treating the fluids as leaky dielectrics, under particular constraints. Traces of this effect remain when σ_1 is further decreased, allowing the second harmonic tongue to remain lower than the first harmonic tongue. The first tongue rises dramatically with each decrease in σ_1, as would be shown by a similar expression to (2.29) upon re-derivation using leaky dielectric fluids.

The departure of the stability curves from the perfect conductor model behaves slightly differently if the permittivity of the bottom fluid is increased. In this case,

https://doi.org/10.1017/jfm.2018.940 Published online by Cambridge University Press

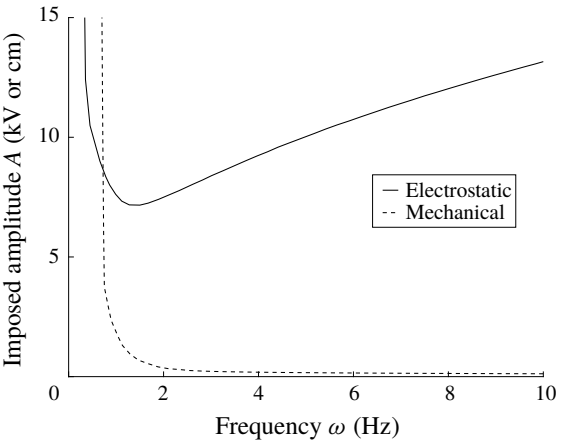


FIGURE 9. Relationship between critical amplitude and forcing frequency for electrostatically (solid) and mechanically (dashed) forced systems. The fluid parameters are given in table 1, with heights of 2.5 cm each. The imposed amplitude is measured in kV for the electrostatic case and cm for the mechanical case. The graph is presented unscaled because of the difference in the physical nature of the amplitudes.

an initial departure from the results of the perfect conductor is still observed with decreasing σ_1. However, the solutions quickly saturate to a new state, where the problem becomes insensitive to σ_1. This phenomenon occurs because of the saturation of the base state charge and voltage profiles, as seen in figure 7(*d*). The saturation approaches the solution to a stacked perfect dielectric system, and is shown in figure 8(*b*) for the same conditions as figure 8(*a*) with ϵ_1 now set to 50.

Behaviour of A with ω

Translating the A versus k stability plots as seen above into plots which relate the critical amplitude of oscillation to the parametric frequency is necessary for experimental validation. This procedure is done by generating a curve similar to that shown in figure 8(*a*) for a wide range of frequencies, and selecting the lowest unstable amplitude available at each of these frequencies. This critical amplitude, and the corresponding wavenumber, are that which will be seen in an experiment for a particular frequency. Generating this curve yields a smooth line which asymptotes to infinity as the frequency approaches zero, and in general decreases with increasing frequency. However, after a certain frequency, increased viscous damping acting on higher wavenumbers causes the curve to begin to rise and increase indefinitely. This is in stark contrast to the behaviour observed for mechanically forced Faraday instability, in which the curve never begins to rise with increasing frequency. (The behaviour in mechanically forced systems was incorrectly reported by Batson, Zoueshtiagh & Narayanan (2013*a*) for low gravity predictions, and in fact never rises so long as any wavenumber is allowable.) Figure 9 shows a comparison between this behaviour in both electrostatically and mechanically forced systems.

This behaviour is a direct result of the distinct physics arising due to the electrostatic nature of the problem. In a mechanically oscillated system, the critical amplitude term is related to a critical acceleration given by $A\omega^2$ which multiplies the density difference between the fluids. The amplitude of acceleration is never encountered by itself, and thus one of the effects of increasing ω is to increase the

https://doi.org/10.1017/jfm.2018.940 Published online by Cambridge University Press

Fluid	Density (kg m^{-3})	Kinematic viscosity (cSt)	Conductivity (S m^{-1})	Relative permittivity	Interfacial tension (kg s^{-2})
Silicone oil	880	1.5	2×10^{-13}	2.36	0.045
Water	1000	1	5.50×10^{-6}	80	

TABLE 1. Summary of fluid properties for the demonstration of critical amplitude dependence on frequency shown in figure 9. The electrical properties play no role in the mechanically forced calculation.

acceleration term, which goes as ω^2. Since this happens, the stabilization from viscous dissipation is overwhelmed with increasing frequency, and the curve asymptotes monotonically. In the electrostatic case, however, the amplitude of voltage oscillation appears independent of frequency, as can be seen explicitly in (2.25). This means that increasing the frequency does not directly increase the terms containing A, and thus viscous dissipation has the opportunity to overcome the typical decrease in threshold with increasing frequency.

Another interesting consequence of the forcing is the impact of the $\Delta\rho$ on the overall system stability. In particular, Faraday instability can only be excited in two-fluid mechanically forced systems with finite $\Delta\rho$ values. Again, this is due to the nature of the amplitude term, which is only found in the form $A\omega^2\Delta\rho$. Naturally, this term vanishes as $\Delta\rho$ disappears, and there is no possibility for Faraday instability to occur. In contrast, the amplitude term in electrostatically forced Faraday instability systems does not multiply $\Delta\rho$, and thus there is still possibility for destabilization when $\Delta\rho$ is set to zero. One must be wary of low wavenumbers in this case if the desired instability is a standing wave, however, as the first tongue solution now shifts to lower amplitudes due to the absence of the gravitational term shown in (2.28). The ability to easily generate Faraday instability in systems with small $\Delta\rho$ values is a definite benefit of electrostatic forcing to mechanical forcing in applications where intentionally exciting the instability could be beneficial to the process, such as microfluidic mixing enhancement (Amiroudine, Zoueshtiagh & Narayanan 2012).

3. Experimental validation of the theory

In order to verify the model, experiments were conducted using a two-fluid system axially constrained by two metallic electrodes, made of aluminium, and laterally bounded by glass walls. Though the testing geometry was laterally bounded, the distance between the walls was large, allowing for comparison to the laterally unbounded theory. Figure 10 shows a schematic of the experimental apparatus, and table 2 gives a summary of the geometry and operating conditions. It should be noted that the measurements within §§ 3 and 4 are reported in unscaled form to give a physical sense of the experimental parameters.

The testing geometry was constructed with top and bottom aluminium plates which enclose the testing cell. The cell itself was constructed from commercially available glass piping. The top and bottom plates were sealed around the testing cell through compression using Buna-N rubber seals and acrylic screws and wing nuts. An overflow port constructed from Delrin plastic was also threaded through the top plate to allow for filling of the cell. A two-fluid system was utilized for all of the experiments by filling the cell through the overflow port until there was direct contact

https://doi.org/10.1017/jfm.2018.940 Published online by Cambridge University Press

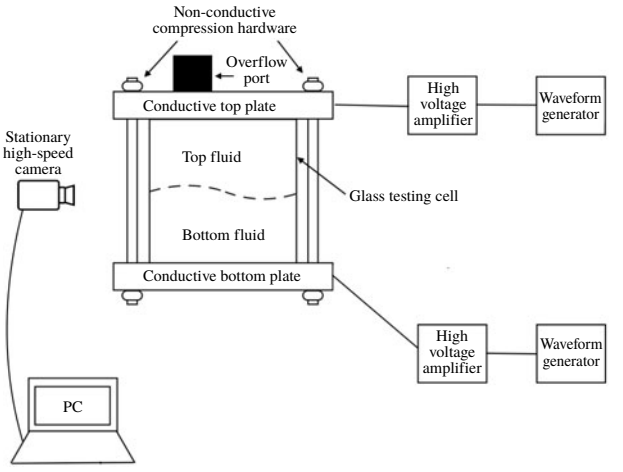


FIGURE 10. Assembled testing cell and experimental set-up. The geometry of choice is sealed between two conductive plates and secured with four non-conductive screws. The top and bottom plates are wired to high voltage amplifiers, and the voltages are controlled using independent signal generators. Backlighting allows for the clear visualization of the interface and any deflection using a high-speed camera.

Label	A	B
Geometry	Cylindrical	Cylindrical
Cross-section	12.7 cm diameter	12.7 cm diameter
Top fluid height	5.1 mm	6.2 mm
Bottom fluid height	33 mm	31.9 mm
Constant voltage offset	0	1 kV

TABLE 2. Summary of the testing geometries and operating conditions. Two tests were conducted using a cylindrical geometry without a constant voltage offset (A) and with a constant voltage offset (B).

between the upper fluid and the upper electrode without any additional air layer. This port also served to provide an additional source of the upper fluid in contact with the inner cell as well as space for the testing fluids to expand. This allowed experiments to be run over long time scales without air bubble generation within the cell. All of the hardware besides the top and bottom plates must be non-conductive for the apparatus to function properly.

Two electrodes were wired to high voltage amplifiers and WAVEFACTORY WF 1943A (top) and 1944A (bottom) signal generators, which were independently controllable by the user. Each electrode was capable of producing voltages up to ± 10 kV. Frequencies in the millihertz to megahertz range were obtainable, though the experiments conducted for the current work utilized frequencies in the 0.5–10 Hz range. The accuracy of the imposed oscillation frequency was $\pm 0.0005\,\%$ and the accuracy of the amplitude varied based on the setpoint, but was typically $\pm 3\,\%$ or better. The electrodes were connected to the top and bottom plates of the testing geometry using alligator clips and a high-speed camera was positioned at an angle slightly above a plane parallel to the interface to allow for viewing of the interface

https://doi.org/10.1017/jfm.2018.940 Published online by Cambridge University Press

in its entirety. Typical experiments included an imposed AC oscillation with set amplitude and frequency on the bottom electrode, while simultaneously holding the upper electrode at a constant voltage.

The fluid choices were based on experimental considerations. In particular, it was found that one fluid needed to be much more conductive than the other in order to make the threshold experimentally obtainable. If both fluids were very non-conductive, then the resulting thresholds became too high to be generated. In addition, short circuits were observed if the amplitude was raised too high, resulting in the generation of bubbles and an automatic shutoff of the high voltage amplifiers for safety. Thus, the most repeatably usable system was ultra-pure water and 1.5 cSt silicone oil, with the majority of the total height being made of the water. The water heights tested were 33 mm and 31.9 mm with corresponding silicone oil heights of 5.1 mm and 6.2 mm, respectively. This allowed for a low critical threshold that was obtainable without inadvertently introducing short circuiting within apparatus.

For the geometries tested in these experiments, the side walls were machined to be far apart to mimic the unbounded nature of the theory. To determine the threshold of the instability, a forcing frequency was selected and an amplitude higher than the threshold was input to examine the responding Faraday waves. The amplitude was slowly decreased until the Faraday modes were no longer seen. This point was determined by measuring the harmonicity of the waves inside the cell. If any single harmonic wave (for $D = 0$) or subharmonic wave (for $D \neq 0$) was observed then the system was taken to be Faraday unstable. The gap between the stable and unstable amplitudes was decreased sequentially until adequate precision (typically 0.1 kV peak to peak) for the threshold amplitude was obtained. The standard time for each experiment was set to be three minutes unless the system became obviously unstable. If the instability did not present itself after three minutes of forcing time, then the tested amplitude was concluded to be within the stable range. As the experimental cells were large enough to behave as unbounded, discrete modes were not obtained during the experiments. Instead, multiple wavelengths were expressed after reaching the threshold for all of the tested frequencies. Due to the camera orientation, the curvature of the glass, and meniscus waves arising due to side wall non-idealities, we were unable to discern the wavelengths to any accuracy, and thus they are not reported. Figure 11 shows the theoretical curve and experimental results for Test A.

For these experiments, the DC offset (D) of the parametric forcing was set to zero. This results in base state meniscus waves that were twice harmonic with the imposed frequency. With an offset of zero, the lowest available Faraday instability tongue is harmonic with the imposed frequency. The agreement between the theory and experiment is excellent when utilizing this geometry and fluid combination. Definite distinction between unstable and stable amplitudes were easily observed with this geometry and operational parameter set. The minimum in the stability curve was exhibited experimentally and the overall behaviour of the theoretical stability curve was confirmed.

Figure 12 depicts the theoretical and experimentally determined threshold amplitudes for Test B, which utilized a non-zero voltage offset. This results in base state meniscus waves that were harmonic with the imposed frequency, and therefore the lowest available Faraday tongue is subharmonic.

As can be seen in figure 12, agreement between the theoretical predictions and experimental data is also reasonable when utilizing a non-zero voltage offset, though not to the same extent as the zero offset case. We conjecture that this is because of imperfections arising due to the presence of a meniscus, despite the fact that the

https://doi.org/10.1017/jfm.2018.940 Published online by Cambridge University Press

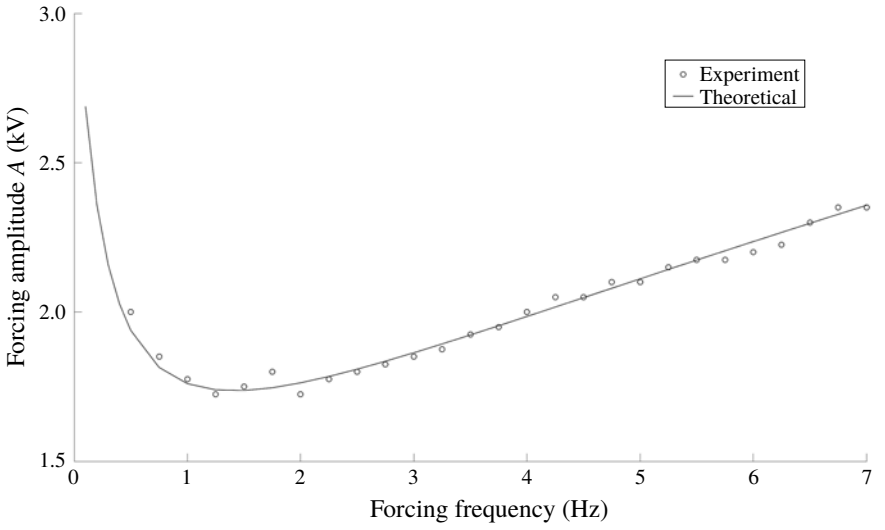


FIGURE 11. Comparison between theoretical and experimental thresholds for Test A. The model is able to capture the experimental threshold accurately over a large frequency range. Threshold amplitudes were measured to the nearest 0.05 kV.

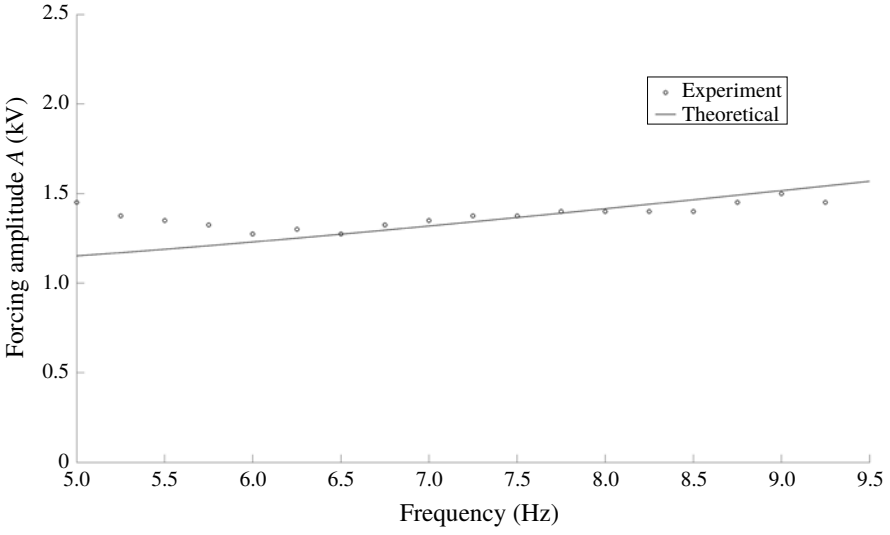


FIGURE 12. Comparison between theoretical and experimental thresholds for Test B. The model is able to predict the instability threshold excellently at high frequency, but interfacial disturbances arising from the DC offset cause discrepancy at lower frequencies. Threshold amplitudes were measured to the nearest 0.05 kV.

container aspect ratio was large. It was observed that even if a pure DC forcing was imposed without an AC component, flow would ensue near the walls and this effect was accentuated by a superimposed AC. Understandably, this imperfection due to the meniscus did not manifest itself as significantly when the DC offset was absent, due to the high frequency of the imposed AC signals. The disturbance

https://doi.org/10.1017/jfm.2018.940 Published online by Cambridge University Press

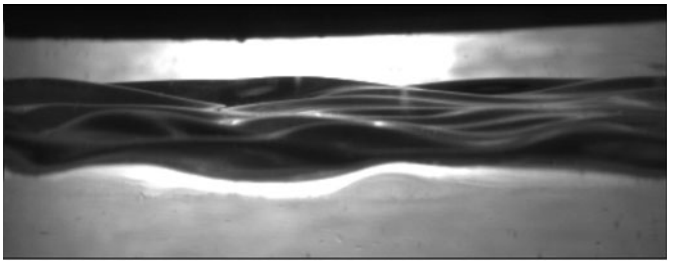


FIGURE 13. Faraday waves obtained during Test A. The frequency and amplitude of forcing are 3.5 Hz and 2.5 kV, respectively. The photograph is taken during the portion of the response cycle with the largest interfacial deflection, and the applied amplitude exceeds the critical threshold.

caused by the DC offset was seemingly magnified at lower frequency, and thus the threshold measurements were only accurately obtainable at higher frequencies. In addition, low frequency experiments offer comparable threshold amplitudes for both subharmonic and harmonic responses. These harmonic responses could compound the noise resulting from the DC offset, thus acting to drown out the subharmonic responses.

Despite these small discrepancies, the experimental data well support the predictions made by the theoretical model for these fluid systems. The agreement is typically best when no voltage offset is imposed. Figure 13 shows an example of Faraday waves obtained during Test A. It can clearly be seen that many wavelengths compete within the cell, but the resulting waveforms are proven to be a result of the Faraday instability due to their response frequency. A supplementary movie, available at https://doi.org/10.1017/jfm.2018.940, shows the temporal behaviour of a typical unstable interface.

4. Measurement of interfacial tension using electrostatically forced Faraday instability

In this section, we show that the electrostatically forced resonant instability is an excellent candidate for the measurement of interfacial tension between liquids, particularly if there is a substantial contrast between their electrical properties. Multiple means for measuring interfacial tension between liquids are currently employed, including both static and dynamic methods. Examples of static methods include the traditional pendant drop tensiometer and Wilhelmy plate (Adamson & Gast 1997), and examples of dynamic methods include the pulse-oscillation technique (Hyers & Rogers 2008). The accurate measurement of interfacial tension is important to a variety of processes, including crystal growth (Schwabe 1988), enhanced oil recovery techniques (Rosen *et al.* 2005; Zhou, Das & Ellis 2016) and space welding (Workman & Kaukler 1989; Fragomeni & Nunes 2003).

The unique nature of electrostatic forcing allows for the imposition of a force which opposes gravity through the constant voltage component of the normal stress (see appendix A). Reduction of the effect of gravity allows interfacial tension to play a more dominant role on the system stability, and thus enables electrostatically forced Faraday instability to be used as a method of interfacial tension measurement. In order to test the accuracy of this measurement method, various interfacial tension values were assumed within the leaky dielectric model and curves of A versus ω

https://doi.org/10.1017/jfm.2018.940 Published online by Cambridge University Press

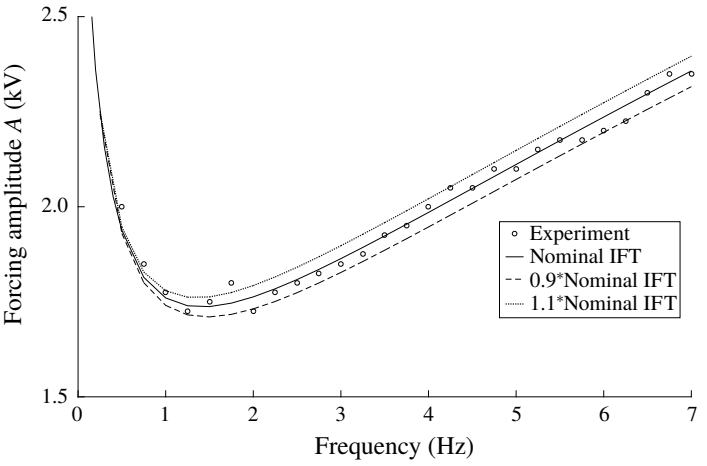


FIGURE 14. Interfacial tension measurement for Si–oil and water system using electrostatic Faraday instability. The solid line represents the nominal interfacial tension, and clearly provides the best fit for the experimental data ($R^2 = 0.978$). Testing properties are those given for figure 11.

were computed. The curve with the closest fit to the experimental data allows us to deduce the interfacial tension between the fluids. Note that the experimental data were presented earlier in figure 11. Figure 14 now shows the same experimental data compared with various theoretical curves where different values of the interfacial tension are assumed.

As can be seen in the figure, the solid line produces the most accurate match of the experimental data. This is the line corresponding to the nominal interfacial tension between the testing fluids (0.045 kg s^{-2}) measured using a KRÜSS DSA100 pendant drop tensiometer. Changing the interfacial tension within the model clearly impacts the predicted stability thresholds, and the effect is substantial enough to be seen experimentally. This study clearly shows that by using interfacial tension as an adjustable parameter within the model to match the experimental data, one would deduce an accurate interfacial tension between the two fluids. This is an important result, as it could potentially serve as a method for the measurement of interfacial tension in systems which behave as electrically conducting pairs such as gallium arsenide superposed by boron oxide, a system found in semiconductor crystal growth processes (Kumar & Subramanian 2015), whose interfacial tension measurement cannot be conveniently made using any of the conventional means. The method complements previous studies on the mechanically (Kumar 1999, 2002; Raynal, Kumar & Fauve 1999; Suman & Kumar 2008) and electrostatically (Espin *et al.* 2013) forced Faraday instabilities utilizing various viscoelastic fluids. The results from these studies suggest that the instability could possibly be harnessed as a characterization method for fluid rheological properties. Again, these types of novel characterization methods could prove valuable for systems exhibiting properties that preclude the use of conventional measurement methods.

5. Conclusions

The Faraday instability or resonant instability is studied theoretically and experimentally for electrostatically forced unconstrained systems. This work is the

https://doi.org/10.1017/jfm.2018.940 Published online by Cambridge University Press

first to report theoretical and experimental observations of the effects of periodic electrostatic forcing on the physics of resonant instability for viscous fluids while accounting for charge dynamics at the interface. The study, which employs classical Floquet instability methods, reveals several results first from a perfect dielectric/perfect conductor model and then from a full leaky dielectric model, culminating in defining, validating experiments.

Multiple observations are made in this study, many of which are new and which arise from the model and the experiments that were conducted. First, it is seen theoretically that the resonant instability that is excited may lead to either subharmonic or harmonic responses depending on the value of the time-independent component of the voltage that is imposed on one of the horizontal bounding walls. These responses are in the shape of 'tongues' in a graph of imposed critical amplitude versus disturbance wavenumber. In particular, it is shown clearly that the subharmonic tongues observed only occur when a non-zero constant voltage offset is added to the oscillatory voltage imposed on the bottom axial wall. In addition, we show that the magnitude of this constant voltage offset strongly influences the shape of the stability tongues and their corresponding critical amplitude values. Second, it is observed that the quadratic nature of the forcing yields another instability tongue – one that can never occur in mechanically forced Faraday instability. This new tongue is entirely due to the time-independent component arising from the quadratic character of the Maxwell stress. Third, it is observed that for systems which exhibit very large conductivity ratios, the leaky dielectric model yields stability thresholds very similar to a simplified perfect conductor model. However, in systems with smaller conductivity ratios, distinct physics are obtained through the use of a leaky dielectric model. In particular, lowering the conductivity of the fluids causes the stability tongues to rise in critical amplitude and shift slightly toward lower wavenumbers. The solutions saturate quickly to the perfect dielectric solutions in the case that the permittivity ratio is also high. Fourth, it is observed that though there are commonalities between the mechanically and electrostatically forced Faraday instability, distinct physics is obtained in the case of electrostatic forcing. For example, an increase in the threshold amplitudes at higher frequencies is observed when utilizing electrostatic forcing, but is entirely absent in mechanical forcing. The electrostatic nature of the forcing also causes the response frequencies to differ from that obtained when utilizing mechanical forcing. These distinctions allow for additional control and manipulation of the electrostatic Faraday instability. Finally, it is concluded that electrostatic forcing, unlike mechanical forcing, can act to counter gravity in a fluid system that is stacked in a gravitationally stable configuration. This observation, in concert with detailed experiments that were conducted to validate the leaky dielectric model, lead us to a novel method to measure interfacial tension. This new method paves the way for new technology to measure this key interfacial property in systems of industrial significance where conventional means cannot be conveniently used.

Acknowledgements

Support is acknowledged from the National Science Foundation via a Graduate Research Fellowship under grant no. DGE-1315138. In addition, K.W. and R.N. acknowledge support from NSF 0968313, CASIS NNH11CD70A, NASA NNX17AL27G, NSF EAPSI 1514711 and Space Florida via the Florida Space Grant Consortium. S.M. acknowledges support from JSPS KAKENHI grant no. JP15H03925.

https://doi.org/10.1017/jfm.2018.940 Published online by Cambridge University Press

Supplementary movie

A supplementary movie is available at https://doi.org/10.1017/jfm.2018.940.

Appendix A. Derivation of the Yih model and the natural frequency when utilizing electrostatic forcing

We begin the re-derivation of the Yih (1968) model by considering a two-fluid system constrained axially between electrodes which impose an oscillatory voltage drop across the fluids, as shown in figure 1. The bottom fluid is considered as an inviscid perfect electrical conductor, and the top fluid is taken as an inviscid perfect dielectric. In this case, the voltage profile in the bottom fluid, i.e. ψ_1 is taken to be constant at $A\cos\omega t$ for all z. The electrostatics in the top fluid are governed by Laplace's equation as shown in § 2.1, and the hydrodynamics in the fluids are governed by the Euler equations coupled with the continuity equation:

$$\rho_j\left(\frac{\partial \boldsymbol{V}_j}{\partial t}+\boldsymbol{V}_j\cdot\boldsymbol{\nabla}\boldsymbol{V}_j\right)=-\boldsymbol{\nabla}P_j-\rho_j g\boldsymbol{i}_z, \tag{A 1}$$

$$\boldsymbol{\nabla}\cdot\boldsymbol{V}_j=0, \tag{A 2}$$

where $\boldsymbol{V}$ is the fluid velocity, P is the pressure, ρ is the density, g is gravitational acceleration and $j=1,2$ denotes the bottom and top fluid, respectively.

The equations are linearized about a quiescent, non-deflecting base state in the usual way by expanding the dependent variables as shown in (2.14). Applying these expansions to (2.1) and (A 1) yields the base state domain equations shown in (2.15) and (2.16), respectively.

Similarly, the perturbation of the domain equations yields (at first order)

$$\rho_j\frac{\partial \boldsymbol{V}_j'}{\partial t}=-\boldsymbol{\nabla}P_j', \tag{A 3}$$

$$\boldsymbol{\nabla}\cdot\boldsymbol{V}_j'=0 \tag{A 4}$$

and

$$\nabla^2\psi_1'=0. \tag{A 5}$$

Velocity is eliminated from the problem by taking $\boldsymbol{\nabla}\cdot$ of each side of (A 3) and utilizing continuity to obtain

$$0=\nabla^2P_j'. \tag{A 6}$$

All the dependent variables are expanded as

$$\phi'(x,z,t)=\mathrm{e}^{\mathrm{i}kx}\tilde{\phi}(z,t), \tag{A 7}$$

where ϕ is any dependent variable. This leads to the expressions for the pressure in both phases,

$$0=\left(\frac{\partial^2}{\partial z^2}-k^2\right)\tilde{P}_j, \tag{A 8}$$

whose solutions take the form

$$\tilde{P}_j=A_j\sinh(kz)+B_j\cosh(kz), \tag{A 9}$$

https://doi.org/10.1017/jfm.2018.940 Published online by Cambridge University Press

as well as the equation and solution for the perturbed voltage profile given by (2.18) and

$$\tilde{\psi}_j = C_j \sinh(kz) + D_j \cosh(kz). \tag{A 10}$$

No-penetration conditions, i.e. $\tilde{V}_{z,j} = 0$, are imposed at both the bounding walls, resulting in

$$\left.\begin{aligned} \frac{\partial \tilde{P}_2}{\partial z} &= 0 \quad \text{at } z = h_2, \\ \frac{\partial \tilde{P}_1}{\partial z} &= 0 \quad \text{at } z = -h_1 \end{aligned}\right\} \tag{A 11}$$

after substitution of these conditions into (A 3).

The usual kinematic condition is applied at the interface,

$$\tilde{W}_j = \frac{\mathrm{d}\tilde{\zeta}}{\mathrm{d}t}, \tag{A 12}$$

which after substitution into (A 3) yields

$$\rho_j \frac{\mathrm{d}^2\tilde{\zeta}}{\mathrm{d}t^2} = -\frac{\partial \tilde{P}_j}{\partial z}. \tag{A 13}$$

The unknown coefficients in (A 9) are determined in terms of $\mathrm{d}^2\tilde{\zeta}/\mathrm{d}t^2$ using (A 13) and (A 11), yielding

$$\left.\begin{aligned} \tilde{P}_1 &= -\frac{\rho_1}{k}\frac{\mathrm{d}^2\tilde{\zeta}}{\mathrm{d}t^2}[\sinh(kz) - \coth(-kh_1)\cosh(kz)], \\ \tilde{P}_2 &= -\frac{\rho_2}{k}\frac{\mathrm{d}^2\tilde{\zeta}}{\mathrm{d}t^2}[\sinh(kz) - \coth(kh_2)\cosh(kz)]. \end{aligned}\right\} \tag{A 14}$$

The problem is closed using the jump momentum balance at order ‘′’,

$$P_2' - P_1' + \zeta'\left(\frac{\mathrm{d}P_2^0}{\mathrm{d}z} - \frac{\mathrm{d}P_1^0}{\mathrm{d}z}\right) = -\gamma k^2\zeta + k\eta(D^2 - 2DA\cos\omega t + \cos^2\omega t)\zeta', \tag{A 15}$$

where $\eta = k\epsilon_2\epsilon_0 \coth kh_2/h_2^2$, which upon inserting the pressure expressions and expanding using (A 7) yields

$$\frac{\mathrm{d}^2\tilde{\zeta}}{\mathrm{d}t^2} + \frac{((\rho_2 - \rho_1)k - \gamma k^3)}{\rho_2 \coth kh_2 + \rho_1 \coth kh_1}\tilde{\zeta} + \frac{k\eta(D^2 - 2DA\cos\omega t + A^2\cos^2\omega t)}{\rho_2 \coth kh_2 + \rho_1 \coth kh_1}\tilde{\zeta} = 0, \tag{A 16}$$

which can be cast into the form of the Mathieu equation

$$\frac{\mathrm{d}^2\tilde{\zeta}}{\mathrm{d}\tau^2} + (p - 2q\cos(2\tau))\tilde{\zeta} = 0 \tag{A 17}$$

https://doi.org/10.1017/jfm.2018.940 Published online by Cambridge University Press

upon the transformations

$$\left.\begin{aligned} D &= -A\cos\omega t, \\ \tau &= \omega t, \\ \sigma_0^2 &= \frac{((\rho_2-\rho_1)k-\gamma k^3)}{\rho_2\coth kh_2+\rho_1\coth kh_1}, \\ \beta &= \frac{2A^2k^2\epsilon_2\epsilon_0\coth kh_2}{h_2^2(\rho_2\coth kh_2+\rho_1\coth kh_1)}, \\ p &= \frac{\sigma_0^2+\beta}{\omega^2}, \\ q &= \frac{\beta}{2\omega^2}. \end{aligned}\right\} \tag{A 18}$$

The natural frequency for an electrostatically forced inviscid two-fluid system can be obtained by first setting $A=0$ in (A 16) and further expanding using

$$\tilde{\phi}(z,t)=\mathrm{e}^{\sigma t}\hat{\phi}(z), \tag{A 19}$$

which yields

$$\sigma^2=-\frac{\left((\rho_1-\rho_2)gk-\dfrac{\epsilon_2\epsilon_0\coth kh_2}{h_2^2}D^2k^2+\gamma k^3\right)}{\rho_2\coth kh_2+\rho_1\coth kh_1}, \tag{A 20}$$

where σ^2 is the natural frequency. It should be noted that the modification to the natural frequency also exists with pure oscillatory forcing (i.e. $D=0$) due to the $A/2$ arising from the application of the double angle formula.

In the absence of electrostatic forcing, the usual natural frequency for a stacked fluid system is comprised of gravitational and interfacial tension contributions, and is given by σ_0^2 in (A 18). These terms are also present within σ^2, along with a modification term due to the Maxwell stress. Due to the fluid orientation, this modification term opposes the gravity and surface tension terms. If the conductive fluid had been located on the top, with all other parameters being equal, the term would have switched signs and acted in conjunction with the typical mechanical terms. Since the nature of Faraday instability revolves around the natural frequency, this is an extremely useful result. In mechanically forced Faraday instability calculations, when using typical density and interfacial tension values, the resulting stability curves are highly independent of the interfacial tension, allowing for order of magnitude changes to the interfacial tension with negligible impact to the system stability. In electrostatically forced Faraday instability, however, tailoring the imposed D value and geometry (k) to oppose gravity can begin to highlight the importance of interfacial tension on the stability thresholds. This can, as shown in § 4, allow for the measurement of interfacial tension using electrostatically forced Faraday instability for certain fluid combinations.

Appendix B. Derivation for the velocity profiles in terms of ζ_n

The theoretical model used for the hydrodynamics in the perfect conductor model is obtained through linear stability analysis, following closely to the model derived

https://doi.org/10.1017/jfm.2018.940 Published online by Cambridge University Press

by Kumar & Tuckerman (1994) with additional Maxwell stress terms within the total stress tensor (see (2.11)). A horizontally infinite two-fluid system is considered, and the hydrodynamics in both fluids are governed by (2.4)–(2.10). It is important to note here the absence of the $\rho_j A\omega^2 \cos \omega t$ term from the right-hand side of (2.4) which is present in mechanically forced Faraday instability problems as a result of adopting a moving reference frame.

These equations are linearized about a quiescent, non-deflecting base state by expanding the dependent variables as shown in (2.14). Applying the expansions yields the base state domain equation

$$\frac{\partial P_{0_j}}{\partial z} = -\rho_j g \tag{B 1}$$

and the perturbed domain equations

$$\left.\begin{gathered} \rho_j \frac{\partial \boldsymbol{V}_j'}{\partial t} = -\boldsymbol{\nabla} P_j' + \mu_j \nabla^2 \boldsymbol{V}_j', \\ \boldsymbol{\nabla} \cdot \boldsymbol{V}_j' = 0. \end{gathered}\right\} \tag{B 2}$$

The double curl is applied to (B 2) to eliminate pressure along with the continuity equation, resulting in

$$\rho_j \partial t \nabla^2 \boldsymbol{V}_j' = \mu_j \nabla^4 \boldsymbol{V}_j'. \tag{B 3}$$

Equation (2.17) is then used to separate variables, resulting in the final perturbed domain equation and its accompanying boundary conditions (dropping hats)

$$\left(\sigma + \mathrm{i}(\alpha + n\omega) - \nu_j \left(\frac{\mathrm{d}^2}{\mathrm{d}z^2} - k^2\right)\right)\left(\frac{\mathrm{d}^2}{\mathrm{d}z^2} - k^2\right) W_{nj} = 0 \tag{B 4}$$

and

$$\left.\begin{gathered} W_{n1} = 0 \quad \text{at } z = -h_1, \\ \frac{\mathrm{d}W_{n1}}{\mathrm{d}z} = 0 \quad \text{at } z = -h_1, \\ W_{n2} = 0 \quad \text{at } z = h_2, \\ \frac{\mathrm{d}W_{n2}}{\mathrm{d}z} = 0 \quad \text{at } z = h_2 \end{gathered}\right\} \tag{B 5}$$

along with the corresponding interfacial conditions at $z = 0$,

$$\left.\begin{gathered} W_{n1} = W_{n2}, \\ \frac{\mathrm{d}W_{n1}}{\mathrm{d}z} = \frac{\mathrm{d}W_{n2}}{\mathrm{d}z}, \\ \mu_1 \left(\frac{\mathrm{d}^2}{\mathrm{d}z^2} + k^2\right) W_{n1} = \mu_2 \left(\frac{\mathrm{d}^2}{\mathrm{d}z^2} + k^2\right) W_{n2}, \\ (\sigma + \mathrm{i}(\alpha + n\omega))\zeta_n = W_{n1}, \end{gathered}\right\} \tag{B 6}$$

where W is the z-component of the perturbed velocity. Equation (B 4) is an ordinary differential equation, whose solution takes the form

$$W_{nj} = A_{nj} \mathrm{e}^{kz} + B_{nj} \mathrm{e}^{-kz} + C_{nj} \mathrm{e}^{q_n z} + D_{nj} \mathrm{e}^{-q_n z}, \tag{B 7}$$

https://doi.org/10.1017/jfm.2018.940 Published online by Cambridge University Press

where $q_n = \sqrt{(\sigma + \mathrm{i}(\alpha + n\omega))/\nu_j + k^2}$. It should be noted that when $q_n = k$, the solution instead takes the form

$$W_{nj} = A_{nj}\mathrm{e}^{kz} + B_{nj}\mathrm{e}^{-kz} + C_{nj}z\mathrm{e}^{kz} + D_{nj}z\mathrm{e}^{-kz}. \tag{B 8}$$

All the unknown coefficients are then calculated by casting the system of equations into matrix form and solving via inversion. Expressions for the velocities in both fluids are now known in terms of ζ_n. The remaining step is to solve the eigenvalue problem derived from the normal component of the stress balance, which ultimately governs the stability of the system:

$$\left[\left[-\left(P' + \zeta'\frac{\mathrm{d}P_0}{\mathrm{d}z}\right) + 2\mu_j\frac{\mathrm{d}W_j}{\mathrm{d}z}\right]\right] + ([[\boldsymbol{T}^{Maxwell}\cdot\boldsymbol{n}]]\cdot\boldsymbol{n})' = -\gamma\nabla_H^2\zeta'. \tag{B 9}$$

Applying $\nabla_H^2\cdot$ to this equation, and substituting the base state pressure term given by (B 1), yields

$$\left[\left[-\nabla_H^2 P' + \nabla_H^2(\rho_j g)\zeta' + 2\mu_j\nabla_H^2\frac{\mathrm{d}W_j}{\mathrm{d}z}\right]\right] + \nabla_H^2([[\boldsymbol{T}^{Maxwell}\cdot\boldsymbol{n}]]\cdot\boldsymbol{n})' = -\gamma\nabla_H^4\zeta'. \tag{B 10}$$

An expression for $\nabla_H^2 P'$ is obtained by combining the continuity equation with $\boldsymbol{\nabla}_H\cdot$ (B 2):

$$\nabla_H^2 P_j' = \left(\rho_j\frac{\partial}{\partial t} - \mu_j\nabla^2\right)\frac{\partial W_j}{\partial z}, \tag{B 11}$$

which upon substitution into (B 10) and expanding variables using (2.17) yields

$$\left[\left[\rho_j(\sigma + \mathrm{i}(\alpha + n\omega))\frac{\partial W_{nj}}{\partial z} - \mu_j\frac{\mathrm{d}^3 W_{nj}}{\mathrm{d}z^3} + k^2\rho_j g\zeta_n + 3\mu_j k^2\frac{\mathrm{d}W_{nj}}{\mathrm{d}z}\right]\right] = \gamma k^4\zeta_n - k^2\tau^{Maxwell}. \tag{B 12}$$

Rearranging (B 12) leads to (2.22), after which the derivation continues in § 2.1.

Appendix C. Expanded matrices for the final eigenvalue problems

The matrices necessary to solve the final eigenvalue problem shown in § 2.1 are constructed separately for the cases of $\alpha = 0$ and $\alpha = \omega/2$. This results in

$$\bar{\boldsymbol{B}} = \begin{bmatrix} B_0^r & -B_0^i & 0 & 0 & 0 & 0 & 0 & 0 & 0 & 0 \\ B_0^i & B_0^r & 0 & 0 & 0 & 0 & 0 & 0 & 0 & 0 \\ 0 & 0 & B_1^r & -B_1^i & 0 & 0 & 0 & 0 & 0 & 0 \\ 0 & 0 & B_1^i & B_1^r & 0 & 0 & 0 & 0 & 0 & 0 \\ 0 & 0 & 0 & 0 & \ddots & \ddots & 0 & 0 & 0 & 0 \\ 0 & 0 & 0 & 0 & \ddots & \ddots & 0 & 0 & 0 & 0 \\ 0 & 0 & 0 & 0 & 0 & 0 & B_{n-1}^r & -B_{n-1}^i & 0 & 0 \\ 0 & 0 & 0 & 0 & 0 & 0 & B_{n-1}^i & B_{n-1}^r & 0 & 0 \\ 0 & 0 & 0 & 0 & 0 & 0 & 0 & 0 & B_n^r & -B_n^i \\ 0 & 0 & 0 & 0 & 0 & 0 & 0 & 0 & B_n^i & B_n^r \end{bmatrix}, \tag{C 1}$$

https://doi.org/10.1017/jfm.2018.940 Published online by Cambridge University Press

$$\bar{\zeta} = \begin{bmatrix} \zeta_0^r \\ \zeta_0^i \\ \zeta_1^r \\ \zeta_1^i \\ \vdots \\ \vdots \\ \zeta_{n-1}^r \\ \zeta_{n-1}^i \\ \zeta_n^r \\ \zeta_n^i \end{bmatrix}, \tag{C 2}$$

$$\bar{\boldsymbol{C}} = C \begin{bmatrix} 1 & 0 & 1 & 0 & 0 & 0 & 0 & 0 & 0 & 0 \\ 0 & -1 & 0 & 1 & 0 & 0 & 0 & 0 & 0 & 0 \\ 1 & 0 & 0 & 0 & 1 & 0 & 0 & 0 & 0 & 0 \\ 0 & 1 & 0 & 0 & 0 & 1 & 0 & 0 & 0 & 0 \\ 0 & 0 & \ddots & 0 & 0 & 0 & \ddots & 0 & 0 & 0 \\ 0 & 0 & 0 & \ddots & 0 & 0 & 0 & \ddots & 0 & 0 \\ 0 & 0 & 0 & 0 & 1 & 0 & 0 & 0 & 1 & 0 \\ 0 & 0 & 0 & 0 & 0 & 1 & 0 & 0 & 0 & 1 \\ 0 & 0 & 0 & 0 & 0 & 0 & 1 & 0 & 0 & 0 \\ 0 & 0 & 0 & 0 & 0 & 0 & 0 & 1 & 0 & 0 \end{bmatrix} \tag{C 3}$$

for $\alpha = \omega/2$, or

$$\bar{\boldsymbol{C}} = C \begin{bmatrix} 0 & 0 & 2 & 0 & 0 & 0 & 0 & 0 & 0 & 0 \\ 0 & 0 & 0 & 0 & 0 & 0 & 0 & 0 & 0 & 0 \\ 1 & 0 & 0 & 0 & 1 & 0 & 0 & 0 & 0 & 0 \\ 0 & 1 & 0 & 0 & 0 & 1 & 0 & 0 & 0 & 0 \\ 0 & 0 & \ddots & 0 & 0 & 0 & \ddots & 0 & 0 & 0 \\ 0 & 0 & 0 & \ddots & 0 & 0 & 0 & \ddots & 0 & 0 \\ 0 & 0 & 0 & 0 & 1 & 0 & 0 & 0 & 1 & 0 \\ 0 & 0 & 0 & 0 & 0 & 1 & 0 & 0 & 0 & 1 \\ 0 & 0 & 0 & 0 & 0 & 0 & 1 & 0 & 0 & 0 \\ 0 & 0 & 0 & 0 & 0 & 0 & 0 & 1 & 0 & 0 \end{bmatrix} \tag{C 4}$$

https://doi.org/10.1017/jfm.2018.940 Published online by Cambridge University Press

for $\alpha = 0$ and

$$\bar{\boldsymbol{E}} = E \begin{bmatrix} 2 & 0 & 1 & 0 & 1 & 0 & 0 & 0 & 0 & 0 \\ 0 & 1 & 0 & -1 & 0 & 1 & 0 & 0 & 0 & 0 \\ 1 & 0 & 2 & 0 & 0 & 0 & 1 & 0 & 0 & 0 \\ 0 & -1 & 0 & 2 & 0 & 0 & 0 & 1 & 0 & 0 \\ 1 & 0 & 0 & 0 & 2 & 0 & 0 & 0 & 1 & 0 \\ 0 & \ddots & 0 & 0 & 0 & \ddots & 0 & 0 & 0 & \ddots \\ 0 & 0 & 1 & 0 & 0 & 0 & 2 & 0 & 0 & 0 \\ 0 & 0 & 0 & 1 & 0 & 0 & 0 & 2 & 0 & 0 \\ 0 & 0 & 0 & 0 & 1 & 0 & 0 & 0 & 2 & 0 \\ 0 & 0 & 0 & 0 & 0 & 1 & 0 & 0 & 0 & 2 \end{bmatrix} \tag{C 5}$$

for $\alpha = (\omega/2)$, or

$$\bar{\boldsymbol{E}} = E \begin{bmatrix} 2 & 0 & 0 & 0 & 2 & 0 & 0 & 0 & 0 & 0 \\ 0 & 2 & 0 & 0 & 0 & 0 & 0 & 0 & 0 & 0 \\ 0 & 0 & 3 & 0 & 0 & 0 & 1 & 0 & 0 & 0 \\ 0 & 0 & 0 & 1 & 0 & 0 & 0 & 1 & 0 & 0 \\ 1 & 0 & 0 & 0 & 2 & 0 & 0 & 0 & 1 & 0 \\ 0 & \ddots & 0 & 0 & 0 & \ddots & 0 & 0 & 0 & \ddots \\ 0 & 0 & 1 & 0 & 0 & 0 & 2 & 0 & 0 & 0 \\ 0 & 0 & 0 & 1 & 0 & 0 & 0 & 2 & 0 & 0 \\ 0 & 0 & 0 & 0 & 1 & 0 & 0 & 0 & 2 & 0 \\ 0 & 0 & 0 & 0 & 0 & 1 & 0 & 0 & 0 & 2 \end{bmatrix} \tag{C 6}$$

for $\alpha = 0$. The matrices necessary to solve the final eigenvalue problem in § 2.3 are constructed in the same manner.

REFERENCES

ABRAMSON, H. N., DODGE, F. T. & KANA, D. 1965 Liquid surface oscillations in longitudinally excited rigid cylindrical containers. *AIAA J.* **3** (4), 685–695.

ADAMSON, A. W. & GAST, A. P. 1997 *Physical Chemistry of Surfaces*, 6th edn. Wiley.

AMIROUDINE, S., ZOUESHTIAGH, F. & NARAYANAN, R. 2012 Mixing generated by Faraday instability between miscible liquids. *Phys. Rev.* E **85**, 016326.

BANDOPADHYAY, A. & HARDT, S. 2017 Stability of horizontal viscous fluid layers in a vertical arbitrary time periodic electric field. *Phys. Fluids* **29**, 124101.

BATSON, W., ZOUESHTIAGH, F. & NARAYANAN, R. 2013*a* Dual role of gravity on the Faraday threshold for immiscible viscous layers. *Phys. Rev.* E **88**, 063002.

BATSON, W., ZOUESHTIAGH, F. & NARAYANAN, R. 2013*b* The Faraday threshold in small cylinders and the sidewall non-ideality. *J. Fluid Mech.* **729**, 496–523.

BECHHOEFER, J., EGO, V., MANNEVILLE, S. & JOHNSON, B. 1995 An experimental study of the onset of parametrically pumped surface waves in viscous fluids. *J. Fluid Mech.* **288** (325–350).

BENJAMIN, T. B. & URSELL, F. 1954 The stability of the plane free surface of a liquid in vertical periodic motion. *Proc. R. Soc. Lond.* A **225** (1163), 505–515.

https://doi.org/10.1017/jfm.2018.940 Published online by Cambridge University Press

BOUKRA, M., CARTELLIER, A., DUCASSE, É., GAJAN, P., LALO, M., NOEL, T. & STRZELECKI, A. 2009 Use of Faraday instabilities to enhance fuel pulverisation in air-blast atomisers. *C. R. Méc.* **337** (6), 492–503.

BRISKMAN, V. A. & SHAIDUROV, G. F. 1968 Parametric instability of a fluid surface in an alternating electric field. *Sov. Phys. Dokl.* **13**, 540–542.

CERDA, E. A. & TIRAPEGUI, E. L. 1998 Faraday's instability in viscous fluid. *J. Fluid Mech.* **368**, 195–228.

CILIBERTO, S. & GOLLUB, J. P. 1985 Chaotic mode competition in parametrically forced surface waves. *J. Fluid Mech.* **158**, 381–398.

CRASTER, R. V. & MATAR, O. K. 2005 Electrically induced pattern formation in thin leaky dielectric films. *Phys. Fluids* **17**, 032104.

DEVITT, E. B. & MELCHER, J. R. 1965 Surface electrohydrodynamics with high-frequency fields. *Phys. Fluids* **8** (6), 1193–1195.

DONG, J., DE ALMEIDA, V. F. & TSOURIS, C. 2001 Formation of liquid columns on liquid–liquid interfaces under applied electric fields. *J. Colloid Interface Sci.* **242**, 327–336.

DOUADY, S. 1990 Experimental study of the Faraday instability. *J. Fluid Mech.* **221**, 383–409.

EDWARDS, W. S. & FAUVE, S. 1994 Patterns and quasi-patterns in the Faraday experiment. *J. Fluid Mech.* **278**, 123–148.

ESPIN, L., CORBETT, A. & KUMAR, S. 2013 Electrohydrodynamic instabilities in thin viscoelastic films: AC and DC fields. *J. Non-Newtonian Fluid Mech.* **196**, 102–111.

FARADAY, M. 1831 On a peculiar class of acoustical figures; and on certain forms assumed by groups of particles upon vibrating elastic surfaces. *Phil. Trans. R. Soc. Lond.* **121**, 299–340.

FRAGOMENI, J. M. & NUNES, A. C. JR 2003 A study of the effects of welding parameters on electron beam welding in the space environment. *Aerosp. Sci. Technol.* **7**, 373–384.

GAMBHIRE, P. & THAOKAR, R. M. 2010 Electrohydrodynamic instabilities at interfaces subjected to alternating electric field. *Phys. Fluids* **22**, 064103.

GAMBHIRE, P. & THAOKAR, R. M. 2012 Role of conductivity in the electrohydrodynamic patterning of air–liquid interfaces. *Phys. Rev.* E **86**, 036301.

HENDERSON, D. M. & MILES, J. W. 1990 Single-mode Faraday waves in small cylinders. *J. Fluid Mech.* **213**, 95–109.

HYERS, R. & ROGERS, J. 2008 A review of electrostatic levitation for materials research. *High Temp. Mater. Process.* **27** (6), 461–474.

IINO, M., SUZUKI, M. & IKUSHIMA, A. 1985 Surface-wave resonance method for measuring surface tension with a very high precision. *J. Phys. Colloq.* **46** (C10), 813–816.

JACQMIN, D. & DUVAL, W. M. B. 1988 Instabilities caused by oscillating accelerations normal to a viscous fluid–fluid interface. *J. Fluid Mech.* **196**, 495–511.

JOHNS, L. & NARAYANAN, R. 2002 *Interfacial Instability*. Springer.

KHORSHIDI, B., JALAAL, M. & ESMAEILZADEH, E. 2011 Electrohydrodynamic instability at the interface between two leaky dielectric fluid layers. *Colloids Surf.* A **380** (1), 207–212.

KUDROLLI, A. & GOLLUB, J. P. 1996 Patterns and spatiotemporal chaos in parametrically forced surface waves: a systematic survey at large aspect ratio. *Physica* D **97** (1), 133–154.

KUMAR, J. & SUBRAMANIAN, C. 2015 Liquid encapsulated Czochralski growth of large size gallium arsenide and indium phosphide single crystals and their characterisation: a review. *IETE J. Res.* **43** (2–3), 125–130.

KUMAR, K. & TUCKERMAN, L. S. 1994 Parametric instability of the interface between two fluids. *J. Fluid Mech.* **279**, 49–68.

KUMAR, S. 1999 Parametrically driven surface waves in viscoelastic liquids. *Phys. Fluids* **11**, 1970–1981.

KUMAR, S. 2002 Vibration-induced interfacial instabilities in viscoelastic fluids. *Phys. Rev.* E **65**, 026305.

MELCHER, J. R. & TAYLOR, G. I. 1969 Electrohydrodynamics: a review of the role of interfacial shear stresses. *Annu. Rev. Fluid Mech.* **1** (1), 111–146.

MÜLLER, H. W. 1993 Periodic triangular patterns in the Faraday experiment. *Phys. Rev. Lett.* **71** (20), 3287–3290.

https://doi.org/10.1017/jfm.2018.940 Published online by Cambridge University Press

OZEN, O., AUBRY, N., PAPAGEORGIOU, D. T. & PETROPOULOS, P. G. 2006 Electrohydrodynamic linear stability of two immiscible fluids in channel flow. *Electrochim. Acta* **51**, 5316–5323.

PEASE, L. F. & RUSSEL, W. B. 2002 Linear stability analysis of thin leaky dielectric films subjected to electric fields. *J. Non-Newtonian Fluid Mech.* **102**, 233–250.

PONTIGA, F. & CASTELLANOS, A. 1994 Physical mechanisms of instability in a liquid layer subjected to an electric field and a thermal gradient. *Phys. Fluids* **6** (5), 1684–1701.

RAYLEIGH, LORD 1883 VII. On the crispations of fluid resting upon a vibrating support. *Phil. Mag.* **16** (97), 50–58.

RAYNAL, F., KUMAR, S. & FAUVE, S. 1999 Faraday instability with a polymer solution. *Eur. Phys. J.* B **9**, 175–178.

REDDY, M. N. & ESMAEELI, A. 2009 The EHD-driven fluid flow and deformation of a liquid jet by a transverse electric field. *Intl J. Multiphase Flow* **35** (11), 1051–1065.

ROBERTS, S. A. & KUMAR, S. 2009 AC electrohydrodynamic instabilities in thin liquid films. *J. Fluid Mech.* **631**, 255–279.

ROBERTS, S. A. & KUMAR, S. 2010 Electrohydrodynamic instabilities in thin liquid trilayer films. *Phys. Fluids* **22** (12), 122102.

ROSEN, M. J., WANG, H., SHEN, P. & ZHU, Y. 2005 Ultralow interfacial tension for enhanced oil recovery at very low surfactant concentrations. *Langmuir* **21** (9), 3749–3756.

SAVILLE, D. A. 1997 Electrohydrodynamics: the Taylor–Melcher leaky dielectric model. *Annu. Rev. Fluid Mech.* **29** (1), 27–64.

SCHWABE, D. 1988 Surface-tension-driven flow in crystal growth melts. In *Superhard Materials, Convection, and Optical Devices*, pp. 75–112. Springer.

SHANKAR, V. & SHARMA, A. 2004 Instability of the interface between thin fluid films subjected to electric fields. *J. Colloid Interface Sci.* **274**, 294–308.

SMORODIN, B. L. & TARAUT, A. V. 2010 Parametric convection of a low-conducting liquid in an alternating electric field. *Fluid Dyn.* **45** (1), 1–9.

STERMAN-COHEN, E., BESTEHORN, M. & ORON, A. 2017 Rayleigh–Taylor instability in thin liquid films subjected to harmonic vibration. *Phys. Fluids* **29**, 052105.

SUMAN, B. & KUMAR, S. 2008 Surfactant- and elasticity-induced inertialess instabilities in vertically vibrated liquids. *J. Fluid Mech.* **610**, 407–423.

TAYLOR, G. I. 1966 Studies in electrohydrodynamics. Part I. The circulation produced in a drop by electrical field. *Proc. R. Soc. Lond.* A **291** (1425), 159–166.

TAYLOR, G. I. & MCEWAN, A. D. 1965 The stability of a horizontal fluid interface in a vertical electric field. *J. Fluid Mech.* **22** (1), 1–15.

TIPTON, C. R. & MULLIN, T. 2004 An experimental study of Faraday waves formed on the interface between two immiscible liquids. *Phys. Fluids* **16** (7), 2336–2341.

TROYON, F. & GRUBER, R. 1971 Theory of the dynamic stabilization of the Rayleigh–Taylor instability. *Phys. Fluids* **14**, 2069–2073.

TSAI, C., MAO, R., TSAI, S., SHAHVERDI, K., ZHU, Y., LIN, S., HSU, Y., BOSS, G., BRENNER, M., MAHON, S. & SMALDONE, G. 2017 Faraday waves-based integrated ultrasonic micro-droplet generator and applications. *Micromachines* **851**, 56–69.

TSAI, S. C. & TSAI, C. S. 2013 Linear theory on temporal instability of megahertz Faraday waves for monodisperse microdroplet ejection. *IEEE Trans. Ultrason. Ferroelectr. Freq. Control* **60** (8), 1746–1755.

TSELUIKO, D. & PAPAGEORGIOU, D. T. 2007 Nonlinear dynamics of electrified thin liquid films. *J. Appl. Maths* **67** (5), 1310–1329.

TSUKAHARA, S., TSURUTA, T. & FUJIWARA, T. 2013 Surface tension determination through measurements of resonance oscillation of a small surface using dielectric force by a localized alternating current electric field. *Analyst* **138**, 2110–2117.

WOLF, G. H. 1970 Dynamic stabilization of the interchange instability of a liquid–gas interface. *Phys. Rev. Lett.* **24** (9), 444–446.

WORKMAN, G. L. & KAUKLER, W. F. 1989 Laser welding in space. Tech. Rep. 19910018227. National Aeronautics and Space Administration.

https://doi.org/10.1017/jfm.2018.940 Published online by Cambridge University Press

YANG, Q., LI, B. Q. & XU, F. 2017 Electrohydrodynamic Rayleigh–Taylor instability in leaky dielectric fluids. *Intl J. Heat Mass Transfer* **109**, 690–704.

YIH, C.S. 1968 Stability of a horizontal fluid interface in a periodic vertical electric field. *Phys. Fluids* **11** (7), 1447–1449.

ZHOU, L., DAS, S. & ELLIS, B. R. 2016 Effect of surfactant adsorption on the wettability alteration of gas-bearing shales. *Environ. Engng Sci.* **33** (10), 766–777.

https://doi.org/10.1017/jfm.2018.940 Published online by Cambridge University Press